

Analytic Nuclear Gradients for Complete Active Space Linearized Pair-Density Functional Theory

Matthew R. Hennefarth,¹ Matthew R. Hermes,¹ Donald G. Truhlar,^{2,*} and Laura Gagliardi^{3,4,†}

¹*Department of Chemistry and Chicago Center for Theoretical Chemistry, University of Chicago, Chicago, IL 60637, USA*

²*Department of Chemistry, Chemical Theory Center, and Minnesota Supercomputing Institute, University of Minnesota, Minneapolis, MN 55455-0431, USA*

³*Department of Chemistry, Pritzker School of Molecular Engineering, The James Franck Institute, and Chicago Center for Theoretical Chemistry, University of Chicago, Chicago, IL 60637, USA*

⁴*Argonne National Laboratory, 9700 S. Cass Avenue, Lemont, IL 60439, USA*

(Dated: March 14, 2024)

Accurately modeling photochemical reactions is difficult due to the presence of conical intersections and locally avoided crossings as well as the inherently multiconfigurational character of excited states. As such, one needs a multi-state method that incorporates state interaction in order to accurately model the potential energy surface at all nuclear coordinates. The recently developed linearized pair-density functional theory (L-PDFT) is a multi-state extension of multiconfiguration PDFT, and it has been shown to be a cost-effective post-MCSCF method (as compared to more traditional and expensive multireference many-body perturbation methods or multireference configuration interaction methods) that can accurately model potential energy surfaces in regions of strong nuclear-electronic coupling in addition to accurately predicting Franck-Condon vertical excitations. In this paper, we report the derivation of analytic gradients for L-PDFT and their implementation in the PYSCF-FORGE software, and we illustrate the utility of these gradients for predicting ground- and excited-state equilibrium geometries and adiabatic excitation energies for formaldehyde, *s-trans*-butadiene, phenol, and cytosine.

I. INTRODUCTION

Accurate characterization and modeling of electronically excited states is important for a variety of chemical and biochemical processes including light-harvesting,^{1–5} photochemistry,^{6,7} photocatalysis,^{8,9} vision,^{10,11} and UV damage to DNA.^{12–14} However, since excited states are typically strongly multiconfigurational, a multireference method is necessary for quantitative and qualitative accuracy. Additionally, since conical intersections and locally avoided crossings are common topological features of excited-state potential energy surfaces, the method should also be able to properly incorporate state interaction so that states of the same symmetry do not unphysically cross or cross on surfaces of the wrong dimensionality.

While state-averaged complete active space self-consistent field (CASSCF) theory^{15,16} is a multireference method that can properly account for static correlation, it does not include dynamic correlation outside of the active space. Multireference many-body perturbation theories such as CAS second-order perturbation theory (CASPT2)¹⁷ or *n*-electron valence state second-order perturbation theory (NEVPT2)¹⁸ are able to recover external dynamic correlation; however, they are computationally very expensive. Multiconfiguration pair-density functional theory (MC-PDFT)^{19–21} is an alternative post-MCSCF approach that combines wave function

theory and density functional theory where the final electronic energy of a multiconfigurational wave function is computed using an on-top energy functional for the non-classical component of the energy. MC-PDFT recovers the missing correlation energy with an accuracy similar to CASPT2²² and NEVPT2²³ but with a significantly reduced computational cost.

MC-PDFT is inaccurate in regions of strong nuclear-electronic coupling because it is a single-state method.^{24–26} Linearized PDFT (L-PDFT)²⁷ is a recently developed multi-state extension of MC-PDFT that incorporates state interaction by defining an effective Hamiltonian that is a functional of a set of densities. It has been shown to be as accurate as extended multi-state CASPT2 (XMS-CASPT2)²⁸ in modeling potential energy surfaces near conical intersections and locally avoided crossings,²⁷ and it is as accurate as NEVPT2 for predicting Franck-Condon vertical excitations.²⁹ L-PDFT also has the benefit of being computationally faster than MC-PDFT since its computational cost is independent of the number of states included in the model space, making it an excellent method to study photochemical reactions and dynamics.

Nuclear gradients are used to optimize molecular geometries to study vertical and adiabatic excitations and to perform molecular dynamics simulations. While it is always possible to calculate gradients numerically, it is often very slow to converge the gradients with respect to the stepsize. Here we report the derivation and implementation of analytic gradients for L-PDFT based on a SA-CASSCF reference wave function. Since the L-PDFT energy is not fully variational with respect to all wave function parameters, we use a Lagrangian-based approach similar to SA-CASSCF gradients,³⁰ SA-MC-

* corresponding author: truhlar@umn.edu

† corresponding author: lgagliardi@uchicago.edu

PDFT gradients,³¹ state-specific MC-PDFT (SS-MC-PDFT) gradients,³² and MC-PDFT gradients with density fitting.³³ We then validate our implementation by comparing the analytic gradients to numerical gradients for the diatomic systems HeH⁺ and LiH. Finally, we show the utility of L-PDFT gradients in predicting both ground- and excited-state geometries, as well as vertical and adiabatic excitation energies for formaldehyde, phenol, *s-trans*-butadiene, and cytosine.

II. THEORY

Throughout this manuscript, lowercase roman letters $p, q, r, s, t, u, v, w, x, y$ indicate general spatial molecular orbitals (MO), and lowercase Greek letters τ, μ, ν, ξ indicate atomic orbital (AO) basis functions. I, J refer to CASSCF eigenstates in the state-averaged space (which is taken to be the same as the model space); Λ, Γ label L-PDFT eigenstates (within the model space); and M, N label CASSCF eigenstates within the complementary part of the state-averaged space (outside the model space). κ is used for MO rotations, λ for general nuclear coordinates, and P for the state-transfer operator. Bold-faced variables are tensors (vectors, matrices, etc.). Einstein summation notation is used throughout (repeated indices are summed implicitly). An efficient implementation of the following equations should make use of the partitioning of orbitals into inactive, active, and virtual, and our code does this; however, our derivation presented in this manuscript does not account for such partitioning for simplicity.

A. L-PDFT

The L-PDFT energy²⁷ of a given state $|\Gamma\rangle$ is defined as the first-order Taylor expansion of the MC-PDFT energy expression¹⁹ in the one- and two-reduced density matrix (RDM) elements around the zero-order density ($\tilde{\gamma}$).

$$E_{\Gamma}^{\text{L-PDFT}} = E^{\text{PDFT}}[\tilde{\gamma}] + \left. \frac{\partial E^{\text{PDFT}}}{\partial \gamma_q^p} \right|_{\tilde{\gamma}} \Delta_q^p + \left. \frac{\partial E^{\text{PDFT}}}{\partial \gamma_{qs}^{pr}} \right|_{\tilde{\gamma}} \Delta_{qs}^{pr} \quad (1)$$

$$\Delta_q^p = \gamma_q^p - \tilde{\gamma}_q^p \quad (2a)$$

$$\Delta_{qs}^{pr} = \gamma_{qs}^{pr} - \tilde{\gamma}_{qs}^{pr} \quad (2b)$$

Here, γ_q^p and γ_{qs}^{pr} are the one- and two-RDM elements of state $|\Gamma\rangle$, $\tilde{\gamma}_q^p$ and $\tilde{\gamma}_{qs}^{pr}$ are the one- and two-RDM elements of the zero-order density, Δ represents the difference in RDM elements between the state $|\Gamma\rangle$ and zero-order density, and $E^{\text{PDFT}}[\tilde{\gamma}]$ is the MC-PDFT energy expression evaluated with the zero-order RDM elements.

$$E^{\text{PDFT}}[\tilde{\gamma}] = h_p^q \tilde{\gamma}_q^p + \frac{1}{2} \mathcal{J}_p^q[\tilde{\gamma}] \tilde{\gamma}_q^p + E^{\text{ot}}[\tilde{\rho}_{\tilde{\gamma}}] + V^{\text{nuc}} \quad (3)$$

$$\mathcal{J}_p^q[\tilde{\gamma}] = g_{pr}^{qs} \tilde{\gamma}_s^r \quad (4)$$

h_p^q and g_{pr}^{qs} are the normal one- and two-electron integrals respectively, V^{nuc} is the nuclear-nuclear repulsion, $\mathcal{J}_p^q[\tilde{\gamma}]$ is the Coulomb interaction of the density $\tilde{\gamma}$, and $E^{\text{ot}}[\tilde{\rho}_{\tilde{\gamma}}]$ is an on-top energy functional that depends on the collective density variables $\tilde{\rho}_{\tilde{\gamma}}$.

$$\tilde{\rho}_{\tilde{\gamma}}^{\top} = [\rho_{\tilde{\gamma}} \quad \Pi_{\tilde{\gamma}} \quad \rho'_{\tilde{\gamma}} \quad \Pi'_{\tilde{\gamma}}] \quad (5)$$

The density (ρ), on-top pair density (Π), and their gradients are generated through the one- and two-RDM elements as

$$\rho_{\tilde{\gamma}} = \phi_p \tilde{\gamma}_q^p \phi^q \quad (6)$$

$$\Pi_{\tilde{\gamma}} = \frac{1}{2} \phi_p \phi_r \tilde{\gamma}_{qs}^{pr} \phi^q \phi^s \quad (7)$$

$$\rho'_{\tilde{\gamma}} = (\phi'_p \phi^q + \phi_p \phi'^q) \tilde{\gamma}_q^p \quad (8)$$

$$\begin{aligned} \Pi'_{\tilde{\gamma}} = & \frac{1}{2} (\phi'_p \phi_r \phi^q \phi^s + \phi_p \phi'_r \phi^q \phi^s \\ & + \phi_p \phi_r \phi'^q \phi^s + \phi_p \phi_r \phi^q \phi'^s) \tilde{\gamma}_{qs}^{pr} \end{aligned} \quad (9)$$

Note that ρ , Π , and ϕ_p are all functions of one three-dimensional variable \mathbf{r} ; and ϕ_p is the p 'th MO. Appendix A describes how the current generation of on-top functionals are evaluated using existing Kohn-Sham (KS) functionals via translated and fully-translated schemes.

The L-PDFT energy is expressible as²⁷

$$\begin{aligned} E_{\Gamma}^{\text{L-PDFT}} = & h_p^q \gamma_q^p + (\mathcal{J}_p^q[\tilde{\gamma}] + V_p^q[\tilde{\rho}_{\tilde{\gamma}}]) \Delta_q^p + \frac{1}{2} v_{pr}^{qs}[\tilde{\rho}_{\tilde{\gamma}}] \Delta_{qs}^{pr} \\ & + E^{\text{ot}}[\tilde{\rho}_{\tilde{\gamma}}] + \frac{1}{2} \mathcal{J}_p^q[\tilde{\gamma}] \tilde{\gamma}_q^p + V^{\text{nuc}} \end{aligned} \quad (10)$$

$$V_p^q = V_p^q[\tilde{\rho}_{\tilde{\gamma}}] = \left. \frac{\partial E^{\text{ot}}}{\partial \gamma_q^p} \right|_{\tilde{\rho}_{\tilde{\gamma}}} \quad (11a)$$

$$v_{pr}^{qs} = v_{pr}^{qs}[\tilde{\rho}_{\tilde{\gamma}}] = 2 \left. \frac{\partial E^{\text{ot}}}{\partial \gamma_{qs}^{pr}} \right|_{\tilde{\rho}_{\tilde{\gamma}}} \quad (11b)$$

The L-PDFT energy contains derivatives of the on-top functional with respect to the one- (V_p^q) and two-RDM (v_{pr}^{qs}) elements (which we call the one- and two-electron on-top potential terms^{31,32}).

In L-PDFT, all functional terms (E^{ot} , V_p^q , v_{pr}^{qs}) are evaluated only at the zero-order density. In practice, the zero-order density is taken to be the weighted average of densities within the state-averaged manifold.

$$\tilde{\gamma}_q^p = \omega_I \langle I | \hat{E}_q^p | I \rangle \quad (12a)$$

$$\tilde{\gamma}_{qs}^{pr} = \omega_I \langle I | \hat{e}_{qs}^{pr} | I \rangle \quad (12b)$$

\hat{E}_q^p and \hat{e}_{qs}^{pr} the one- and two-electron excitation operators respectively. We take ω_I to be the same weight as in the underlying SA-CASSCF or state-averaged complete active space configuration interaction calculation. For the analytic L-PDFT gradients, we require equal weights ($\omega_I = \omega_J$) so that the zero-order density is invariant to rotation among states within the model space, as is done in SA-CASSCF.³⁰ We do not expect the limitation of L-PDFT analytical gradients to equal weights to impact the applicability of the method because almost all implemented SA-CASSCF analytical gradients also require equal weights in order to exploit the energy invariance to rotations within the state-averaged space.

Because the L-PDFT energy depends linearly on the one- and two-RDM elements of the state, it is possible to express it as the expectation value of a Hermitian operator which we call the L-PDFT Hamiltonian ($\hat{H}^{\text{L-PDFT}}$).

$$E_{\Gamma}^{\text{L-PDFT}} = \langle \Gamma | \hat{H}^{\text{L-PDFT}} | \Gamma \rangle \quad (13)$$

$$\hat{H}^{\text{L-PDFT}} = (h_p^q + \mathcal{J}_p^q[\tilde{\gamma}] + V_p^q) \hat{E}_q^p + \frac{1}{2} v_{pr}^{qs} \tilde{\gamma}_{qs}^{pr} + h^{\text{const}} \quad (14)$$

Here h^{const} is a constant term that only depends on $\tilde{\gamma}$.

$$h^{\text{const}} = V^{\text{nuc}} + E^{\text{ot}} - \left(\frac{1}{2} \mathcal{J}_p^q[\tilde{\gamma}] + V_p^q \right) \tilde{\gamma}_q^p - \frac{1}{2} v_{pr}^{qs} \tilde{\gamma}_{qs}^{pr} \quad (15)$$

The final L-PDFT energies and states are the solutions to the eigenvalue equation of the operator $\hat{H}^{\text{L-PDFT}}$ projected within the model space spanned by the eigenvectors of the underlying SA-CASSCF calculation.

$$|\Gamma\rangle \langle \Gamma | \hat{H}^{\text{L-PDFT}} | \Lambda \rangle = \delta_{\Gamma}^{\Lambda} E_{\Lambda}^{\text{L-PDFT}} |\Gamma\rangle \quad (16)$$

Note that $|\Gamma\rangle$ and $|I\rangle$ span the same model space, but the state $|I\rangle$ are chosen such that they diagonalize the normal electronic Hamiltonian projected within that space.

B. The L-PDFT Energy Lagrangian

The Hellmann-Feynman theorem^{34–36} implies that if an energy E is stationary with respect to all parameters defining the wave function ($|\Psi\rangle$), then

$$\frac{dE}{d\lambda} = \langle \Psi | \frac{d\hat{H}}{d\lambda} | \Psi \rangle \quad (17)$$

As such, one does not have to account for the response of the wave function to a change in nuclear coordinate (λ).

The L-PDFT energy is not stationary with respect to MO rotations and state rotations out of the model space; hence, the Hellmann-Feynman theory cannot be applied. However, one can avoid calculating the response of the wave function with respect to a nuclear displacement by using Lagrange's method of undetermined multipliers. This requires us to enumerate the variables defining

the wave function and the systems of equations that set them to their particular values.

Similarly to SA-CASSCF, the final L-PDFT eigenstates can be parameterized as

$$|\Gamma\rangle = e^{\hat{P}^{\Gamma}} e^{\hat{\kappa}} |0\rangle \quad (18)$$

where $\hat{\kappa}$ is the orbital rotation operator

$$\hat{\kappa} = \sum_{p < q} \kappa_p^q \left[\hat{\mathbf{E}} - \hat{\mathbf{E}}^{\dagger} \right]_q^p \quad (19)$$

and \hat{P}^{Γ} is the state transfer operator for state $|\Gamma\rangle$. \hat{P}^{Γ} can be decomposed into rotations within the model space ($\hat{P}_{\parallel}^{\Gamma}$) and those outside the model space (\hat{P}_{\perp}^{Γ}).

$$\hat{P}^{\Gamma} = \hat{P}_{\perp}^{\Gamma} + \hat{P}_{\parallel}^{\Gamma} \quad (20)$$

$$\hat{P}_{\perp}^{\Gamma} = P_M^{\Gamma} (|M\rangle \langle \Gamma| - |\Gamma\rangle \langle M|) \quad (21)$$

$$\hat{P}_{\parallel}^{\Gamma} = P_{\Lambda}^{\Gamma} (|\Lambda\rangle \langle \Gamma| - |\Gamma\rangle \langle \Lambda|) \quad (22)$$

Since our reference wave function comes from a SA-CASSCF calculation, the parameters κ_p^q and P_M^{Γ} are optimized with respect to the SA-CASSCF energy (E^{SA}).

$$\frac{\partial E^{\text{SA}}}{\partial \kappa_p^q} = 0 \quad (23)$$

$$\frac{\partial E^{\text{SA}}}{\partial P_M^{\Gamma}} = 0 \quad (24)$$

The P_{Λ}^{Γ} parameters are determined by diagonalizing $\hat{H}^{\text{L-PDFT}}$, which is equivalent to making the energies stationary with respect to interstate rotations.

$$\frac{\partial E_{\Gamma}^{\text{L-PDFT}}}{\partial P_{\Lambda}^{\Gamma}} = 0 \quad (25)$$

For equal weights, E^{SA} is invariant to rotation within the model space, and hence

$$\frac{d}{dx} \left(\frac{\partial E^{\text{SA}}}{\partial P_{\Lambda}^{\Gamma}} \right) = 0 \quad (26)$$

for any parameter x .³⁰

Our constraints are given by Eqs. 23 and 24; therefore, our Lagrangian for state $|\Gamma\rangle$ takes the form

$$\mathcal{L}_{\Gamma} = E_{\Gamma}^{\text{L-PDFT}} + \bar{\kappa} \cdot \nabla_{\kappa} E^{\text{SA}} + \bar{\mathbf{P}}^{\perp} \cdot \nabla_{\mathbf{P}^{\perp}} E^{\text{SA}} \quad (27)$$

As a reminder $\bar{\kappa}$ and $\bar{\mathbf{P}}^{\perp}$ are the associated Lagrange multipliers for the orbital rotations and state rotations out of the model space respectively. Both $\bar{\kappa}$ and $\bar{\mathbf{P}}^{\perp}$ are

determined by making the Lagrangian stationary with respect to κ_p^q and P_M^Λ .

$$\frac{\partial \mathcal{L}_\Gamma}{\partial \kappa_p^q} = 0 = \frac{\partial \mathcal{L}_\Gamma}{\partial P_M^\Lambda} \quad (28)$$

As indicated by Eqs. 25 and 26, \mathcal{L}_Γ is already invariant to rotations within the model space, and therefore does not need to be accounted for. Substituting Eq. 27 into Eq. 28 yields a system of coupled linear equations.

$$\begin{bmatrix} \nabla_{\kappa} E_\Gamma^{\text{L-PDFT}} \\ \nabla_{\mathbf{P}^\perp} E_\Gamma^{\text{L-PDFT}} \end{bmatrix} = - \begin{bmatrix} \mathbf{H}_{\kappa\kappa}^{E^{\text{SA}}} & \mathbf{H}_{\kappa\mathbf{P}^\perp}^{E^{\text{SA}}} \\ \mathbf{H}_{\mathbf{P}^\perp\kappa}^{E^{\text{SA}}} & \mathbf{H}_{\mathbf{P}^\perp\mathbf{P}^\perp}^{E^{\text{SA}}} \end{bmatrix} \begin{bmatrix} \bar{\kappa} \\ \bar{\mathbf{P}}^\perp \end{bmatrix} \quad (29)$$

The left-hand side is the energy response of the L-PDFT energy, and the first factor on the right is the Hessian of E^{SA} with respect to κ_p^q and P_M^Λ ; these terms will be discussed in Section II C. Equations 27 and 29 are almost identical to those presented in the SA-CASSCF analytic gradients,³⁰ with the difference being that the wave function energy response terms on the left side have been replaced with the L-PDFT energy response terms. As such, Eq. 29 can be solved using the standard SA-CASSCF preconditioned conjugate gradient iterative solver.^{37,38}

C. Energy Response

The SA-CASSCF Hessian that appears in Eq. 29 is well established^{30,39} and unchanged in this derivation. In practice, we evaluate $\mathbf{H}^{E^{\text{SA}}}$ within the L-PDFT eigenstate basis, rather than the SA-CASSCF eigenstate basis, which slightly modifies the form of the equation as is described in Appendix B.

As seen on the left side of Eq. 29, we need the response of the L-PDFT energy with respect to orbital and CI rotations. However, it is important to realize that $E_\Gamma^{\text{L-PDFT}}$ depends on the model space, and changing either the orbitals or CI parameters for any state within the model space changes the zero-order density. Hence, we break each component into an explicit and implicit part; the explicit part represents the response of only the state, whereas the implicit part accounts for changes due to the zero-order density.

1. Explicit Dependence

The derivatives of γ with respect to κ_p^q are given by

$$\frac{\partial \gamma_q^p}{\partial \kappa_x^y} = (\delta_x^p \gamma_y^p + \delta_x^p \gamma_q^y) - (\delta_y^p \gamma_x^p + \delta_y^p \gamma_q^x) \quad (30a)$$

$$\begin{aligned} \frac{\partial \gamma_{qs}^{pr}}{\partial \kappa_x^y} &= (\delta_x^p \gamma_{qs}^{yr} + \delta_x^p \gamma_{ys}^{pr} + \delta_x^r \gamma_{qs}^{py} + \delta_x^s \gamma_{qs}^{pr}) \\ &\quad - (\delta_y^p \gamma_{qs}^{xr} + \delta_y^p \gamma_{xs}^{pr} + \delta_y^r \gamma_{qs}^{px} + \delta_y^s \gamma_{qs}^{pr}) \end{aligned} \quad (30b)$$

Therefore,

$$\frac{\partial E_\Gamma^{\text{L-PDFT}}}{\partial \gamma} \cdot \frac{\partial \gamma}{\partial \kappa_x^y} = 2[\mathcal{F}_{\text{ex}} - \mathcal{F}_{\text{ex}}^\dagger]_y^x \quad (31)$$

where \mathcal{F}_{ex} is the explicit part of the L-PDFT generalized Fock matrix.

$$[\mathcal{F}_{\text{ex}}]_y^x = (h_y^q + \mathcal{J}_y^q[\tilde{\gamma}] + V_y^q) \gamma_q^x + v_{yr}^{qs} \gamma_{qs}^{xr} \quad (32)$$

The derivative of γ with respect to P_M^Λ is given by

$$\frac{\partial \gamma_q^p}{\partial P_M^\Lambda} = 2\delta_\Lambda^\Gamma \gamma_{\Lambda q}^{Mp} \quad (33a)$$

$$\frac{\partial \gamma_{qs}^{pr}}{\partial P_M^\Lambda} = 2\delta_\Lambda^\Gamma \gamma_{\Lambda qs}^{Mpr} \quad (33b)$$

where $\gamma_{\Lambda q}^{Mp}$ and $\gamma_{\Lambda qs}^{Mpr}$ are the transition density matrix elements from $|M\rangle$ to $|\Lambda\rangle$.

$$\gamma_{\Lambda q}^{Mp} = \langle \Lambda | \hat{E}_q^p | M \rangle \quad (34a)$$

$$\gamma_{\Lambda qs}^{Mpr} = \langle \Lambda | \hat{e}_{qs}^{pr} | M \rangle \quad (34b)$$

Therefore, the explicit response of the L-PDFT energy to state rotations out of the model space is given by

$$\frac{\partial E_\Gamma^{\text{L-PDFT}}}{\partial \gamma} \cdot \frac{\partial \gamma}{\partial P_M^\Lambda} = 2\delta_\Lambda^\Gamma \langle \Lambda | \hat{H}^{\text{L-PDFT}} | M \rangle \quad (35)$$

In general, these expressions are similar to the SA-CASSCF response equations³⁰ but with modified one- and two-electron integrals.

2. Implicit Dependence

Since the L-PDFT energy directly depends on the first derivatives of E^{ot} with respect to γ , the energy response involves explicit second derivatives. We define the elements of the Hessian of E^{ot} with respect to the RDM elements as

$$F_{p,r}^{q,s} = \left. \frac{\partial^2 E^{\text{ot}}}{\partial \gamma_q^p \partial \gamma_r^s} \right|_{\bar{\rho}_\gamma} \quad (36a)$$

$$F_{p,rt}^{q,su} = F_{rt,p}^{su,q} = 2 \left. \frac{\partial^2 E^{\text{ot}}}{\partial \gamma_q^p \partial \gamma_{su}^{rt}} \right|_{\bar{\rho}_\gamma} \quad (36b)$$

$$F_{pr,tv}^{qs,uw} = 4 \left. \frac{\partial^2 E^{\text{ot}}}{\partial \gamma_{qs}^{pr} \partial \gamma_{uv}^{tw}} \right|_{\bar{\rho}_\gamma} \quad (36c)$$

Since E^{ot} is the integral of the on-top kernel (ϵ^{ot}) over all space,

$$E^{\text{ot}}[\bar{\rho}] = \int \epsilon^{\text{ot}}[\bar{\rho}(\mathbf{r})] d\mathbf{r} \quad (37)$$

we can move the derivatives of Eq. 36 inside the integral. Applying the chain rule twice gives

$$\mathbf{F} = \begin{bmatrix} \{F_{p,t}^{q,u}\} & \{F_{pr,t}^{qs,u}\} \\ \{F_{t,pr}^{u,qs}\} & \{F_{pr,tv}^{qs,uw}\} \end{bmatrix} \quad (38)$$

$$= \int d\mathbf{r} \begin{bmatrix} \frac{\partial \bar{\rho}}{\partial \gamma_q^p} \\ \frac{\partial \bar{\rho}}{\partial \gamma_{qs}^{pr}} \end{bmatrix} \cdot \mathbf{f}^{\text{ot}} \cdot \left[\left\{ \frac{\partial \bar{\rho}}{\partial \gamma_u^t} \right\} \quad 2 \left\{ \frac{\partial \bar{\rho}}{\partial \gamma_{uv}^{tw}} \right\} \right]$$

$$\frac{\partial \bar{\rho}}{\partial \gamma_q^p} = \begin{bmatrix} \phi_p \phi^q \\ 0 \\ 2\phi'_p \phi^q \\ 0 \end{bmatrix} \quad (39a)$$

$$\frac{\partial \bar{\rho}}{\partial \gamma_{qs}^{pr}} = \frac{1}{2} \begin{bmatrix} 0 \\ \phi_p \phi_r \phi^q \phi^s \\ 0 \\ 4\phi'_p \phi_r \phi^q \phi^s \end{bmatrix} \quad (39b)$$

where \mathbf{f}^{ot} is the Hessian of the on-top potential kernel with elements

$$\mathbf{f}^{\text{ot}} = \begin{bmatrix} \frac{\partial^2 \epsilon^{\text{ot}}}{\partial \rho^2} & \frac{\partial^2 \epsilon^{\text{ot}}}{\partial \rho \partial \Pi} & \frac{\partial^2 \epsilon^{\text{ot}}}{\partial \rho \partial \rho'} & \frac{\partial^2 \epsilon^{\text{ot}}}{\partial \rho \partial \Pi'} \\ \frac{\partial^2 \epsilon^{\text{ot}}}{\partial \rho \partial \Pi} & \frac{\partial^2 \epsilon^{\text{ot}}}{\partial \Pi^2} & \frac{\partial^2 \epsilon^{\text{ot}}}{\partial \Pi \partial \rho'} & \frac{\partial^2 \epsilon^{\text{ot}}}{\partial \Pi \partial \Pi'} \\ \frac{\partial^2 \epsilon^{\text{ot}}}{\partial \rho \partial \rho'} & \frac{\partial^2 \epsilon^{\text{ot}}}{\partial \Pi \partial \rho'} & \frac{\partial^2 \epsilon^{\text{ot}}}{\partial \rho'^2} & \frac{\partial^2 \epsilon^{\text{ot}}}{\partial \rho' \partial \Pi'} \\ \frac{\partial^2 \epsilon^{\text{ot}}}{\partial \rho \partial \Pi'} & \frac{\partial^2 \epsilon^{\text{ot}}}{\partial \Pi \partial \Pi'} & \frac{\partial^2 \epsilon^{\text{ot}}}{\partial \rho' \partial \Pi'} & \frac{\partial^2 \epsilon^{\text{ot}}}{\partial \Pi'^2} \end{bmatrix} \quad (40)$$

See Appendix D for a description of how \mathbf{f}^{ot} is evaluated.

As we will see, \mathbf{F} is always contracted with the Δ density elements. We define the Hessian-vector product $\Delta \cdot \mathbf{F}$ to be the on-top gradient response.

$$[\Delta \cdot \mathbf{F}]_t^u = F_{p,t}^{q,u} \Delta_q^p + \frac{1}{2} F_{pr,t}^{qs,u} \Delta_{qs}^{pr} \quad (41a)$$

$$[\Delta \cdot \mathbf{F}]_{tv}^{uw} = F_{p,tv}^{q,uw} \Delta_q^p + \frac{1}{2} F_{pr,tv}^{qs,uw} \Delta_{qs}^{pr} \quad (41b)$$

We directly compute the elements of $\Delta \cdot \mathbf{F}$ on the grid by moving the contraction with Δ within the integral, thereby avoiding constructing tensors of up to rank 8. We see this by first noting that the density variables $\bar{\rho}$ are linear with respect to the RDM elements

$$\bar{\rho}_\Delta = \frac{\partial \bar{\rho}}{\partial \gamma_q^p} \Delta_q^p + \frac{\partial \bar{\rho}}{\partial \gamma_{qs}^{pr}} \Delta_{qs}^{pr} = \frac{\partial \bar{\rho}}{\partial \gamma} \cdot \Delta \quad (42)$$

Thus, contracting Eq. 38 with the elements of the Δ , we find that the elements of $\Delta \cdot \mathbf{F}$ are given by

$$[\Delta \cdot \mathbf{F}]_p^q = \int d\mathbf{r} \bar{\rho}_\Delta^\top \cdot \mathbf{f}^{\text{ot}} \cdot \frac{\partial \bar{\rho}}{\partial \gamma_q^p} \quad (43a)$$

$$[\Delta \cdot \mathbf{F}]_{pr}^{qs} = 2 \int d\mathbf{r} \bar{\rho}_\Delta^\top \cdot \mathbf{f}^{\text{ot}} \cdot \frac{\partial \bar{\rho}}{\partial \gamma_{qs}^{pr}} \quad (43b)$$

The derivative of the $E_\Gamma^{\text{L-PDFT}}$ with respect to the zero-order density matrix elements is given by

$$\frac{\partial E_\Gamma^{\text{L-PDFT}}}{\partial \gamma_u^t} = \mathcal{J}_t^u[\Delta] + [\Delta \cdot \mathbf{F}]_t^u \quad (44a)$$

$$\frac{\partial E_\Gamma^{\text{L-PDFT}}}{\partial \gamma_{uv}^{tw}} = \frac{1}{2} [\Delta \cdot \mathbf{F}]_{tv}^{uw} \quad (44b)$$

Using Eq. 30, we see that the L-PDFT energy implicit response to MO rotations is

$$\frac{\partial E_\Gamma^{\text{L-PDFT}}}{\partial \tilde{\gamma}} \cdot \frac{\partial \tilde{\gamma}}{\partial \kappa_x^y} = 2 \left[\mathcal{F}_{\text{impl}} - \mathcal{F}_{\text{impl}}^\dagger \right]_y^x \quad (45)$$

where $\mathcal{F}_{\text{impl}}$ is the implicit contribution to the L-PDFT generalized Fock matrix.

$$[\mathcal{F}_{\text{impl}}]_y^x = \left(\mathcal{J}_y^q[\Delta] + [\Delta \cdot \mathbf{F}]_y^q \right) \tilde{\gamma}_q^x + [\Delta \cdot \mathbf{F}]_{yr}^{qs} \tilde{\gamma}_{qs}^{xr} \quad (46)$$

Additionally, if we consider Eq. 33, we find that

$$\frac{\partial \tilde{\gamma}_q^p}{\partial P_M^\Lambda} = 2\omega_\Lambda \gamma_{\Lambda q}^{Mp} \quad (47a)$$

$$\frac{\partial \tilde{\gamma}_{qs}^{pr}}{\partial P_M^\Lambda} = 2\omega_\Lambda \gamma_{\Lambda qs}^{Mpr} \quad (47b)$$

Therefore, we have that the implicit response of $E_\Gamma^{\text{L-PDFT}}$ to state rotations out of the model space is given by

$$\frac{\partial E_\Gamma^{\text{L-PDFT}}}{\partial \tilde{\gamma}} \cdot \frac{\partial \tilde{\gamma}}{\partial P_M^\Lambda} = 2\omega_\Lambda G_\Lambda^M \quad (48)$$

where we have defined G_Λ^M as

$$G_\Lambda^M = \langle \Lambda | \hat{G} | M \rangle \quad (49)$$

$$\hat{G} = \left(\mathcal{J}_p^q[\Delta] + [\Delta \cdot \mathbf{F}]_p^q \right) \hat{E}_q^p + \frac{1}{2} [\Delta \cdot \mathbf{F}]_{pr}^{qs} \hat{e}_{qs}^{pr} \quad (50)$$

3. Response Summary

Given the above decompositions, we have the L-PDFT energy response to orbitals rotations is given by

$$\frac{\partial E_\Gamma^{\text{L-PDFT}}}{\partial \kappa_x^y} = 2 \left[\mathcal{F} - \mathcal{F}^\dagger \right]_y^x \quad (51)$$

where \mathcal{F} is the full L-PDFT generalized Fock matrix.

$$\begin{aligned} \mathcal{F}_y^x &= [\mathcal{F}_{\text{ex}} + \mathcal{F}_{\text{impl}}]_y^x \\ &= (h_y^q + \mathcal{J}_y^q[\tilde{\gamma}] + V_y^q) \gamma_q^x + v_{yr}^{qs} \gamma_{qs}^{xr} \\ &\quad + \left(\mathcal{J}_y^q[\Delta] + [\Delta \cdot \mathbf{F}]_y^q \right) \tilde{\gamma}_q^x + [\Delta \cdot \mathbf{F}]_{yr}^{qs} \tilde{\gamma}_{qs}^{xr} \end{aligned} \quad (52)$$

Additionally, we have that the L-PDFT energy response to state rotations out of the model space is given by

$$\frac{\partial E_\Gamma^{\text{L-PDFT}}}{\partial P_M^\Lambda} = 2 \left(\delta_\Lambda^\Gamma \left[\hat{H}^{\text{L-PDFT}} \right]_\Lambda^M + \omega_\Lambda G_\Lambda^M \right) \quad (53)$$

Note that when there is only one state within the model space, $\tilde{\gamma} \rightarrow \gamma$ and the L-PDFT energy is exactly the same as the SS-MC-PDFT energy. Correspondingly, one can see that all of the implicit terms would vanish from Eqs. 52 and 53, which would result in the same response equations as derived for the SS-MC-PDFT gradients.³¹

D. Derivative of the Lagrangian

Having solved for the Lagrange multipliers in Eq. 27 via Eq. 29, the gradient of \mathcal{L}_Γ yields the same gradient as fully differentiating $E_\Gamma^{\text{L-PDFT}}$. Differentiating Eq. 27 with respect to nuclear displacements yields

$$\begin{aligned} \frac{d\mathcal{L}_\Gamma}{d\lambda} &= \frac{dE_\Gamma^{\text{L-PDFT}}}{d\lambda} \\ &= \langle \Gamma | \frac{d\hat{H}^{\text{L-PDFT}}}{d\lambda} | \Gamma \rangle + \bar{\boldsymbol{\kappa}} \cdot \nabla_{\boldsymbol{\kappa}} \left(\omega_\Lambda \langle \Lambda | \frac{d\hat{H}^{\text{el}}}{d\lambda} | \Lambda \rangle \right) \\ &\quad + \bar{\mathbf{P}}^\perp \cdot \nabla_{\mathbf{P}^\perp} \left(\omega_\Lambda \langle \Lambda | \frac{d\hat{H}^{\text{el}}}{d\lambda} | \Lambda \rangle \right) \end{aligned} \quad (54)$$

Both the electronic Hamiltonian and the L-PDFT Hamiltonian in Eq. 54 are expressed within second quantization, which requires that the MOs always be orthonormal. A change in nuclear coordinates can cause the underlying MOs to no longer be orthogonal. In particular, if we consider the following AO to MO transformation at a fixed geometry (λ_0),

$$|\phi^p; \lambda_0\rangle = C_\mu^p |\phi^\mu; \lambda_0\rangle \quad (55)$$

then for any slight nuclear displacement δ , the overlap between the perturbed MOs at this perturbed geometry is no longer orthonormal.

$$\langle \phi_p; \lambda_0 + \delta | \phi^q; \lambda_0 + \delta \rangle \neq \delta_p^q \quad (56)$$

To ensure that our MOs are orthogonal regardless of the geometry, we introduce the orthogonal molecular orbital (OMO) picture⁴⁰ (using the Löwdin orthonormalization⁴¹),

$$|\psi^{\bar{p}}; \lambda\rangle = \left[\mathbf{S}^{-\frac{1}{2}}(\lambda) \right]_{\bar{p}}^p C_\mu^p |\phi^\mu; \lambda\rangle \quad (57)$$

where $\mathbf{S}(\lambda)$ is the overlap matrix in the MO basis

$$S_q^p(\lambda) = \langle \phi_q; \lambda | \phi^p; \lambda \rangle \quad (58)$$

At the reference geometry ($\lambda = \lambda_0$), the OMOs are the same as the MOs since $\mathbf{S}(\lambda_0)$ is the identity matrix. Equation 57 also highlights that the transformation from AOs to OMOs also depends on the nuclear coordinates. The derivatives of the one- and two-electron integrals in the OMO basis are given by

$$\frac{dh_{\bar{p}}^{\bar{q}}}{d\lambda} = h_{p,\lambda}^q - \frac{1}{2} \left(S_{p,\lambda}^x h_x^q + S_{x,\lambda}^q h_p^x \right) \quad (59)$$

$$\frac{dg_{\bar{p}\bar{r}}^{\bar{q}\bar{s}}}{d\lambda} = g_{pr,\lambda}^{qs} - \frac{1}{2} \left(S_{p,\lambda}^x g_{xr}^{qs} + S_{r,\lambda}^x g_{px}^{qs} + S_{x,\lambda}^q g_{pr}^{xs} + S_{x,\lambda}^s g_{pr}^{qx} \right) \quad (60)$$

where $h_{p,\lambda}^q$ and $g_{pr,\lambda}^{qs}$ are the derivatives of the one- and two-electron integrals in the MO basis, and $S_{q,\lambda}^p$ is the

derivative of the overlap matrix element. The term involving the derivative of the overlap elements is often called the ‘‘connection’’ or ‘‘renormalization’’ contribution. The one- and two-electron derivative integrals and the overlap matrix elements are obtained in the AO basis as

$$h_{\tau,\lambda}^\mu = \langle \phi_{\tau,\lambda} | \hat{h} | \phi^\mu \rangle + \left\langle \phi_\tau \left| \hat{h} \right| \phi_{,\lambda}^\mu \right\rangle + \langle \phi_\tau | \frac{\partial \hat{h}}{\partial \lambda} | \phi^\mu \rangle \quad (61)$$

$$\begin{aligned} g_{\tau\nu,\lambda}^{\mu\xi} &= \langle \phi_{\tau,\lambda} \phi_\nu | \hat{g} | \phi^\mu \phi^\xi \rangle + \langle \phi_\tau \phi_{\nu,\lambda} | \hat{g} | \phi^\mu \phi^\xi \rangle \\ &\quad + \left\langle \phi_\tau \phi_\nu \left| \hat{g} \right| \phi_{,\lambda}^\mu \phi^\xi \right\rangle + \left\langle \phi_\tau \phi_\nu \left| \hat{g} \right| \phi^\mu \phi_{,\lambda}^\xi \right\rangle \end{aligned} \quad (62)$$

$$S_{\tau,\lambda}^\mu = \langle \phi_{\tau,\lambda} | \phi^\mu \rangle + \left\langle \phi_\tau \left| \phi_{,\lambda}^\mu \right\rangle \quad (63)$$

where $\phi_{\tau,\lambda}$ represents the partial derivative of ϕ_τ with respect to the nuclear coordinate.

$$\phi_{\tau,\lambda} = \frac{\partial \phi_\tau}{\partial \lambda} \quad (64)$$

Within the L-PDFT Hamiltonian, there are no explicit two-electron integrals, but only Coulomb integrals. The Coulomb derivative integrals, generated from a density γ , are given by

$$\mathcal{J}_{p,\lambda}^q[\gamma] = \left(\langle \phi_{p,\lambda} \phi_r | \hat{g} | \phi^q \phi^s \rangle + \langle \phi_p \phi_r | \hat{g} | \phi^{q,\lambda} \phi^s \rangle \right) \gamma_s^r \quad (65)$$

The derivative of the Coulomb contribution can be rewritten in terms of the Coulomb derivative integrals. For example,

$$\begin{aligned} \frac{\partial \mathcal{J}_p^q[\tilde{\gamma}]}{\partial \lambda} \Delta_q^p &= g_{pr,\lambda}^{qs} \tilde{\gamma}_s^r \Delta_q^p \\ &= \mathcal{J}_{p,\lambda}^q[\tilde{\gamma}] \Delta_q^p + \mathcal{J}_{p,\lambda}^q[\Delta] \tilde{\gamma}_q^p \end{aligned} \quad (66)$$

Since the on-top energy and on-top potential terms depend on the collective density variables (which are constructed from the OMOs), they will also give a renormalization contributions.^{31,32}

$$\frac{dE_{,\lambda}^{\text{ot}}}{d\lambda} = E_{,\lambda}^{\text{ot}} - S_{x,\lambda}^y \left(V_y^p \tilde{\gamma}_p^x + v_{yr}^{qs} \tilde{\gamma}_{qs}^{xr} \right) \quad (67)$$

$$\frac{dV_{\bar{p}}^{\bar{q}}}{d\lambda} \Delta_{\bar{q}}^{\bar{p}} = V_{p,\lambda}^q \Delta_q^p - S_{x,\lambda}^y \left(V_y^p \Delta_x^p + [\Delta \cdot \mathbf{F}]_y^p \tilde{\gamma}_p^x \right) \quad (68a)$$

$$\frac{dv_{\bar{p}\bar{r}}^{\bar{q}\bar{s}}}{d\lambda} \Delta_{\bar{q}\bar{s}}^{\bar{p}\bar{r}} = v_{pr,\lambda}^{qs} \Delta_{qs}^{pr} - 2S_{x,\lambda}^y \left(v_{yr}^{qs} \Delta_{qs}^{xr} + [\Delta \cdot \mathbf{F}]_{yr}^{qs} \tilde{\gamma}_{qs}^{xr} \right) \quad (68b)$$

The explicit derivatives of the on-top energy ($E_{,\lambda}^{\text{ot}}$) and one- and two-electron on-top potentials ($V_{p,\lambda}^q$ and $v_{pr,\lambda}^{qs}$) can be evaluated in various forms since the tensor contractions can be performed in different orders. Here we present the derivatives as they are implemented in our

PYSCF-FORGE implementation. The nuclear derivative of the collective density variables can be written as

$$\frac{\partial \bar{\rho}_\gamma^\top}{\partial \lambda} = \left[\frac{\partial \rho_\gamma}{\partial \lambda} \quad \frac{\partial \Pi_\gamma}{\partial \lambda} \quad \frac{\partial \rho'_\gamma}{\partial \lambda} \quad \frac{\partial \Pi'_\gamma}{\partial \lambda} \right] + \delta_\lambda(\mathbf{r}) \nabla \bar{\rho}_\gamma \cdot \bar{\mathbf{n}}_\lambda \quad (69)$$

$$\frac{\partial \rho_\gamma}{\partial \lambda} = 2\phi_p \gamma_q^p \phi_q^q \quad (70)$$

$$\frac{\partial \Pi_\gamma}{\partial \lambda} = 2\phi_{p,\lambda} \phi_r \gamma_{qs}^{pr} \phi^q \phi^s \quad (71)$$

$$\frac{\partial \rho'_\gamma}{\partial \lambda} = 2 \left(\phi'_{p,\lambda} \phi^q + \phi'_p \phi_{,\lambda}^q \right) \gamma_q^p \quad (72)$$

$$\frac{\partial \Pi'_\gamma}{\partial \lambda} = 2 \left(\phi'_{p,\lambda} \phi_r \phi^q \phi^s + 3\phi'_p \phi_{r,\lambda} \phi^q \phi^s \right) \gamma_{qs}^{pr} \quad (73)$$

where $\delta_\lambda(\mathbf{r})$ is 1 if \mathbf{r} is evaluated at a grid point associated with the atom of the coordinate λ and is 0 otherwise, and $\bar{\mathbf{n}}_\lambda$ is the Cartesian unit vector for the coordinate direction λ . The explicit derivative of the on-top energy with respect to nuclear coordinates is given as

$$E_{,\lambda}^{\text{ot}} = \int d\mathbf{r} \left(\mathbf{v}^{\text{ot}} \cdot \frac{\partial \bar{\rho}_\gamma}{\partial \lambda} \right) + \{ \epsilon^{\text{ot}} \}_{\mathbf{r} \in \mathcal{G}} \cdot \frac{\partial \bar{w}}{\partial \lambda} \quad (74)$$

where \mathcal{G} is the set of all grid points, \bar{w} is the corresponding set of quadrature weights, \mathbf{v}^{ot} is the derivative of the on-top kernel with respect to the density variables,

$$\mathbf{v}^{\text{ot}} = \nabla_{\bar{\rho}} \epsilon^{\text{ot}} = \left[\frac{\partial \epsilon^{\text{ot}}}{\partial \rho} \quad \frac{\partial \epsilon^{\text{ot}}}{\partial \Pi} \quad \frac{\partial \epsilon^{\text{ot}}}{\partial \rho'} \quad \frac{\partial \epsilon^{\text{ot}}}{\partial \Pi'} \right] \quad (75)$$

and

$$\{ \epsilon^{\text{ot}} \}_{\mathbf{r} \in \mathcal{G}}^\top = [\epsilon^{\text{ot}}(\mathbf{r}_1) \quad \epsilon^{\text{ot}}(\mathbf{r}_2) \quad \dots \quad \epsilon^{\text{ot}}(\mathbf{r}_n)] \quad (76)$$

is the on-top kernel evaluated at every grid point (as a vector). See Appendix C for how \mathbf{v}^{ot} is evaluated. The nuclear derivative of the on-top potential is given as

$$V_{p,\lambda}^q = \int d\mathbf{r} \left(\frac{\partial \bar{\rho}^\top}{\partial \gamma_q^p} \cdot \mathbf{f}^{\text{ot}} \cdot \frac{\partial \bar{\rho}_\gamma}{\partial \lambda} + \mathbf{v}^{\text{ot}} \cdot \frac{\partial^2 \bar{\rho}}{\partial \gamma_q^p \partial \lambda} \right) + \left\{ \mathbf{v}^{\text{ot}} \cdot \frac{\partial \bar{\rho}}{\partial \gamma_q^p} \right\}_{\mathbf{r} \in \mathcal{G}} \cdot \frac{\partial \bar{w}}{\partial \lambda} \quad (77a)$$

$$v_{pr,\lambda}^{qs} = 2 \int d\mathbf{r} \left(\frac{\partial \bar{\rho}^\top}{\partial \gamma_{qs}^{pr}} \cdot \mathbf{f}^{\text{ot}} \cdot \frac{\partial \bar{\rho}_\gamma}{\partial \lambda} + \mathbf{v}^{\text{ot}} \cdot \frac{\partial^2 \bar{\rho}}{\partial \gamma_{qs}^{pr} \partial \lambda} \right) + 2 \left\{ \mathbf{v}^{\text{ot}} \cdot \frac{\partial \bar{\rho}}{\partial \gamma_{qs}^{pr}} \right\}_{\mathbf{r} \in \mathcal{G}} \cdot \frac{\partial \bar{w}}{\partial \lambda} \quad (77b)$$

However, because the density variables are linear with respect to the RDM elements (Eq. 42), we can move the contraction with Δ in Eq. 68 within the integral (just like in Eq. 43). Additionally, to reduce quadrature loops, we evaluate the on-top energy derivative at the same time

such that the nuclear derivative due to all on-top terms is given as

$$\begin{aligned} E_{,\lambda}^{\text{ot}} + V_{p,\lambda}^q \Delta_q^p + \frac{1}{2} v_{pr,\lambda}^{qs} \Delta_{qs}^{pr} \\ = \int d\mathbf{r} \left(\bar{\rho}_\Delta^\top \cdot \mathbf{f}^{\text{ot}} \cdot \frac{\partial \bar{\rho}_\gamma}{\partial \lambda} + \mathbf{v}^{\text{ot}} \cdot \frac{\partial \bar{\rho}_\gamma}{\partial \lambda} \right) \\ + \{ \epsilon^{\text{ot}} + \mathbf{v}^{\text{ot}} \cdot \bar{\rho}_\Delta \}_{\mathbf{r} \in \mathcal{G}} \cdot \frac{\partial \bar{w}}{\partial \lambda} \end{aligned} \quad (78)$$

We can therefore write the full gradient of the L-PDFT energy for state $|\Gamma\rangle$ as

$$\begin{aligned} \frac{dE_\Gamma^{\text{L-PDFT}}}{d\lambda} = \langle \Gamma | \frac{d\hat{H}^{\text{L-PDFT}}}{d\lambda} | \Gamma \rangle \\ + h_{p,\lambda}^q \check{\gamma}_q^p + \frac{1}{2} g_{pr,\lambda}^{qs} \check{\gamma}_{qs}^{pr} - S_{x,\lambda}^y \check{\mathcal{F}}_y^x \end{aligned} \quad (79)$$

where $\check{\gamma}$ are the effective RDM elements, which contain the Lagrange multiplier terms as

$$\check{\gamma}_q^p = (\check{\gamma}_q^x \bar{\kappa}_x^p - \check{\gamma}_x^p \bar{\kappa}_q^x) + \omega^\Lambda \bar{P}_M^\Lambda \left[\hat{\mathbf{E}} + \hat{\mathbf{E}}^\dagger \right]_{\Lambda q}^{Mp} \quad (80a)$$

$$\begin{aligned} \check{\gamma}_{qs}^{pr} = (\check{\gamma}_{qs}^{xr} \bar{\kappa}_x^p - \check{\gamma}_{xs}^{pr} \bar{\kappa}_q^r + \check{\gamma}_{qs}^{px} \bar{\kappa}_r^x - \check{\gamma}_{qx}^{pr} \bar{\kappa}_s^x) \\ + \omega^\Lambda \bar{P}_M^\Lambda \left[\hat{\mathbf{e}} + \hat{\mathbf{e}}^\dagger \right]_{\Lambda qs}^{Mpr} \end{aligned} \quad (80b)$$

and $\check{\mathcal{F}}$ is the effective Fock matrix,

$$\check{\mathcal{F}}_\tau^\mu = h_\tau^\nu \check{\gamma}_\nu^\mu + g_{\tau\eta}^{\nu\xi} \check{\gamma}_{\nu\xi}^{\mu\eta} \quad (81)$$

The L-PDFT Hellmann-Feynman contribution is given as

$$\begin{aligned} \langle \Gamma | \frac{d\hat{H}^{\text{L-PDFT}}}{d\lambda} | \Gamma \rangle = h_{p,\lambda}^q \check{\gamma}_q^p + \mathcal{J}_{p,\lambda}^q [\check{\gamma}] \Delta_q^p + \mathcal{J}_{p,\lambda}^q [\gamma] \check{\gamma}_q^p \\ + V_{,\lambda}^{\text{nuc}} + E_{,\lambda}^{\text{ot}} + V_{p,\lambda}^q \Delta_q^p + \frac{1}{2} v_{pr,\lambda}^{qs} \Delta_{qs}^{pr} \\ - S_{x,\lambda}^y \mathcal{F}_y^x \end{aligned} \quad (82)$$

where \mathcal{F} is the generalized L-PDFT Fock matrix (defined in Eq. 52). Equations 80 and 81 are essentially the same as those that appear in other Lagrange-based analytic gradient approaches.^{30-32,52}

III. COMPUTATIONAL METHODS

All calculations used PYSCF^{53,54} (Version 2.3, commit v1.1-8104-g6c1ea86eb) compiled with the LIBXC^{55,56} (Version 6.1.0) and LIBCINT⁵⁷ (Version 6.0.0) libraries, MRH⁵⁸ (commit SHA-1 b3185fe), and PYSCF-FORGE⁵⁹ (commit SHA-1 c503f41). Geometry optimizations were performed with the GEOMETRIC⁶⁰ package (version 1.0) within PYSCF. All PDFT calculations used a numerical quadrature grid size of 6 (80/120 radial points and 770/974 angular points for atoms of periods 1/2 respectively). All L-PDFT calculations used the model

TABLE I. Systems studied along with the symmetry, basis set, number of states (N), number of active electrons (n_e), active space orbitals, and the on-top functional used.

System	Sym. ^a	Basis Set	N	n_e	Active Orbitals	Functional
HeH ⁺	C_1	cc-pVDZ ⁴²	2	2	σ, σ^*	tPBE ^{19,43} ftSVWN3 ^b
LiH	C_1	aug-cc-pVTZ ^{42,48}	2	2	σ, σ^*	tPBE ^{19,43} ftPBE ^{43,44}
formaldehyde	C_1	jun-cc-pVTZ ^{42,48-51}	2	12	full valence	tPBE ^{19,43}
<i>s-trans</i> -butadiene	C_{2h}	jul-cc-pVTZ ^{42,48-51}	2 (1A_g)	4	$2(\pi, \pi^*)$	tPBE ^{19,43}
phenol	C_1	jul-cc-pVDZ ^{42,48-51}	3	12	$3(\pi, \pi^*), p_z$ of O	tPBE ^{19,43}
cytosine	C_s	jul-cc-pVTZ ^{42,48-51}	3 ($^1A'$)	14	$\sigma_{OH}, \sigma_{OH}^*, \sigma_{CO}, \sigma_{CO}^*$ $5\pi, 3\pi^*$, and 2 lone-pairs	tPBE ^{19,43}

^a Point group symmetry

^b ftSVWN3 is a fully-translated⁴⁴ local-spin-density approximation with the exchange functional being the one called Slater exchange^{45,46} in LIBXC and the correlation functional being correlation functional number 3 of Vosko *et al.*⁴⁷.

space spanned by the SA-CASSCF eigenvectors to construct \hat{H}^{L-PDFT} and equal weights ($\omega_I = \omega_J$). System-specific computational details including symmetry, basis set, number of states in the model space, active space, and on-top functional used are summarized in Table I.

Numerical gradients were computed using the central difference method. Because there is a dependence on the step size (δ), we calculated numerical gradients with differing δ and extrapolated to the $\delta \rightarrow 0$ limit. Specifically, a linear regression of the numerical gradient versus δ^2 is performed for a subset of data where the correlation coefficient R^2 is greater than 0.9, and the y -intercept is taken to be the extrapolated numerical gradient.

Both numerical and analytic gradients suffer from numerical error since they rely on a wave function that is only converged to finite precision. For all comparisons between analytic and numerical gradients, we use an energy convergence threshold of 10^{-12} hartree and an orbital and CI rotation gradient threshold of 10^{-6} . For convenience, we will refer to the numerical gradient as the reference for the rest of this manuscript (as we have done previously^{32,61}). We also define the unsigned error (UE) (in units of hartree/bohr) and relative error (RE) (unitless) as

$$UE = |\text{Analytic} - \text{Numerical}| \quad (83)$$

$$RE = \left| \frac{\text{Analytic} - \text{Numerical}}{\text{Numerical}} \right| \quad (84)$$

IV. RESULTS AND DISCUSSION

A. Validation of Analytic Gradients Using Diatomic Molecules

We first test our analytic gradient implementation with translated and fully-translated functionals at a variety of points on the potential energy curves of two diatomic systems: HeH⁺⁶²⁻⁶⁶ and LiH.⁶⁷⁻⁷¹ Analytic and numerical

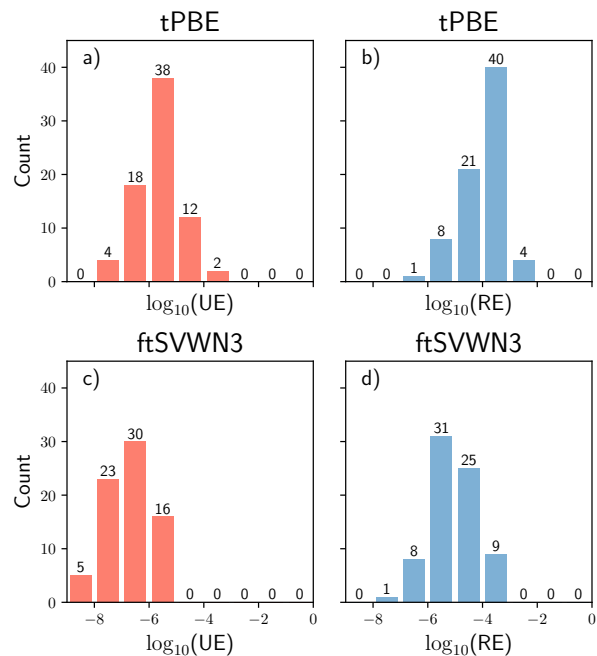


FIG. 1. Distribution of the common log of the unsigned (a,c) and relative (b,d) error of analytic gradients relative to numerical gradients for all states of HeH⁺ at various internuclear distances. The top row (a,b) is using the tPBE functional and bottom row (c,d) is using the ftSVWN3 functional.

gradients were computed for interatomic distances in the range 0.4 Å to 4.0 Å with a step size of 0.1 Å. As both the common log of UE and RE occur in roughly standard distributions, we present the errors as histograms.

HeH⁺ is the simplest possible system for which many terms in the programmable equations for L-PDFT analytic gradients do not vanish due to symmetry. The $\log_{10}(UE)$ and $\log_{10}(RE)$ distributions for both the tPBE and ftSVWN3 functional are shown in Fig. 1. For the tPBE functional, the majority of the UEs are below

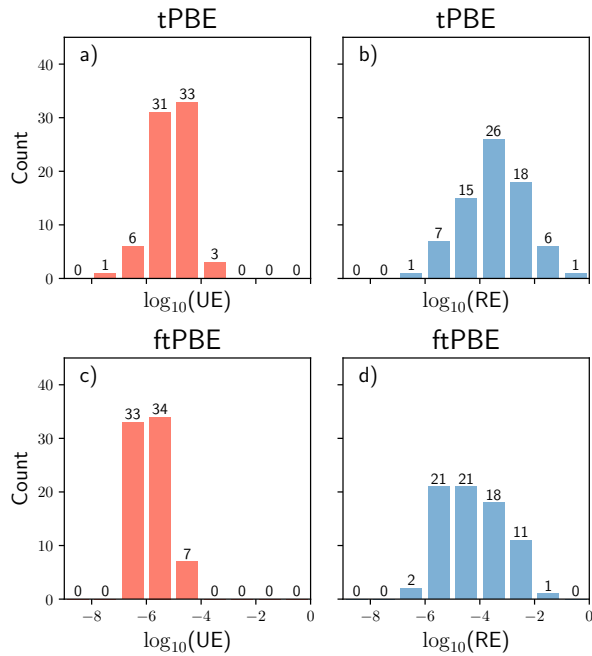


FIG. 2. Distribution of the common log of the unsigned (a,c) and relative (b,d) error of analytic gradients relative to numerical gradients for all states of LiH at various internuclear distances. The top row (a,b) is for the tPBE functional, and the bottom row (c,d) is for the ftPBE functional.

1×10^{-5} hartree/bohr whereas for the ftSVWN3 functional they are below 1×10^{-6} hartree/bohr. The RE is fairly constant throughout the potential energy curve for both functionals (Fig. S1 and S2) with the RE for tPBE being an order of magnitude greater than for ftSVWN3.

The $\log_{10}(\text{UE})$ and $\log_{10}(\text{RE})$ distributions using both the tPBE and ftPBE functionals for the lowest two $^1\Sigma^+$ states of LiH are summarized in Fig. 2. We see that the majority of UEs are below 1×10^{-4} hartree/bohr for tPBE and below 1×10^{-5} hartree/bohr for ftPBE. There are slightly larger REs for both functionals in the dissociation region of the potential energy curve (Figs. S3 and S4) which are likely due to the flatness of the potential. For example, the largest REs for tPBE and ftPBE occur on the upper $^1\Sigma^+$ state at 2.7 Å and 2.8 Å with analytic gradients of 1.7532×10^{-3} hartree/bohr and 9.0825×10^{-5} hartree/bohr respectively.

Table II summarizes the statistical agreement between the analytic and numerical gradients for both systems and all functionals. Overall, tPBE has mean unsigned error (MUE) of 1.4×10^{-5} hartree/bohr and 2.5×10^{-5} hartree/bohr for HeH⁺ and LiH respectively; these are consistent with our previous implementations of MC-PDFT gradients. There, we saw that the analytic and numerical gradients for LiH computed with tPBE and CMS-tPBE had MUEs of 4×10^{-5} hartree/bohr³² and 4.9×10^{-5} hartree/bohr⁶¹ respectively.

The fully-translated functionals have better agreement

TABLE II. Mean signed error (MSE), mean unsigned error (MUE), and root-mean-squared error (RMSE) of the analytic gradients relative to the numerical gradients. All values are in hartree/bohr.

Functional	HeH ⁺		LiH	
	tPBE	ftSVWN3	tPBE	ftPBE
MSE	2.2×10^{-6}	-1.2×10^{-7}	-3.8×10^{-6}	5.3×10^{-7}
MUE	1.4×10^{-5}	9.0×10^{-7}	2.5×10^{-5}	4.4×10^{-6}
RMSE	5.1×10^{-5}	1.9×10^{-6}	5.1×10^{-5}	9.1×10^{-6}

with the numerical gradients for both HeH⁺ and LiH (Table II). This can likely be attributed to the fact that translated functionals have a discontinuity in the first derivative of the translation scheme (where values of R in Eq. A9 equal 1); and since L-PDFT gradients require the second derivative, this discontinuity leads to larger numerical instabilities. The fully-translated functionals, on the other hand, use a polynomial interpolation to avoid the discontinuity (Appendix A), and this likely leads to more accurate gradients.

Overall, we find good agreement between the analytic and numerical gradients at all geometries considered for both HeH⁺ and LiH using both translated and fully-translated functionals.

B. Formaldehyde

Here we consider calculations with a full-valence active space of the optimized ground state (S_0) and the first excited state of $n \rightarrow \pi^*$ character (S_1) of formaldehyde. In the ground state, formaldehyde is a planar molecule with C_{2v} symmetry. For the first excited state of formaldehyde, it is known that the C=O double bond is elongated, and the molecule is no longer planar. We chose to not enforce symmetry for two reasons: (i) One planned application of L-PDFT is to photochemistry. In photochemical simulations, one needs globally continuous potential energy surfaces, but if one enforces symmetry at high-symmetry points, one will usually get discontinuities between high-symmetry points and low-symmetry points. So we do not enforce symmetry in photochemical simulations, and the present paper is testing L-PDFT in that context. (ii) The only way to include both states within the state-averaged manifold in OPENMOLCAS⁷² is to not enforce symmetry. Not enforcing symmetry allows us to be consistent with our prior study of formaldehyde using SA-CASSCF, SA-PDFT, and compressed multi-state PDFT (CMS-PDFT) which used the OPENMOLCAS quantum chemistry package.^{32,61}

We define η to be the angle between the H-C-H plane and the C=O bond, which is a measure of the nonplanarity of the structure. We will take as our reference the experimental ground- and excited-state geometries reported by Duncan⁷³ and Jensen and Bunker⁷⁴ respectively.

TABLE III. L-PDFT ground and first excited state bond lengths, bond angles, and out-of-plane angle (η) for formaldehyde compared with various methods. All bond lengths are in Å and all angles are in degrees. Experimental uncertainty shown in parentheses.

State	Method	Basis Set	r_{CO}	r_{CH}	θ_{HCH}	η
S_0	L-PDFT(12,10)	jun-cc-pVTZ	1.210	1.115	116.4	0
	SA-CASSCF(12,12) ³²	aug-cc-pVTZ	1.214	1.103	117.3	0
	MC-PDFT(12,12) ³²	aug-cc-pVTZ	1.210	1.114	116.1	0
	MC-PDFT(6,5) ⁶¹	jun-cc-pVTZ	1.202	1.112	115.8	0
	CMS-PDFT(6,5) ⁶¹	jun-cc-pVTZ	1.203	1.112	115.8	0
	CASPT2(12,10) ⁷⁵	aug-cc-pVTZ	1.209	1.102	116.1	0
	ADC(2) ⁷⁵	aug-cc-pVTZ	1.209	1.096	116.5	0
	CCSD ⁷⁵	aug-cc-pVTZ	1.201	1.097	116.4	0
	CCSDR(3) ⁷⁵	aug-cc-pVTZ	1.207	1.100	116.4	0
	CC2 ⁷⁵	aug-cc-pVTZ	1.217	1.098	116.4	0
	CC3 ⁷⁵	aug-cc-pVTZ	1.208	1.100	116.2	0
	expt. ⁷³		1.207(1)	1.117(1)	116.2(1)	0
S_1	L-PDFT(12,10)	jun-cc-pVTZ	1.328	1.100	118.1	34.5
	SA-CASSCF(12,12) ³²	aug-cc-pVTZ	1.356	1.079	118.1	32
	MC-PDFT(12,12) ³²	aug-cc-pVTZ	1.323	1.102	117.6	28
	MC-PDFT(6,5) ⁶¹	jun-cc-pVTZ	1.333	1.095	119.9	30
	CMS-PDFT(6,5) ⁶¹	jun-cc-pVTZ	1.333	1.095	119.9	30
	CASPT2(12,10) ⁷⁵	aug-cc-pVTZ	1.326	1.090	118.1	38
	ADC(2) ⁷⁵	aug-cc-pVTZ	1.380	1.081	123.8	19
	CCSD ⁷⁵	aug-cc-pVTZ	1.300	1.087	118.9	30.9
	CCSDR(3) ⁷⁵	aug-cc-pVTZ	1.320	1.089	118.2	37
	CC2 ⁷⁵	aug-cc-pVTZ	1.353	1.085	121.3	29.5
	CC3 ⁷⁵	aug-cc-pVTZ	1.326	1.089	118.3	32.7
	expt. ⁷⁴		1.323(3)	1.103(1)	118.1(1)	34

The L-PDFT ground- and excited-state structural parameters are summarized in Table III, where they are compared to results obtained by other methods including MC-PDFT³² and CASPT2.⁷⁵ Both the MC-PDFT and CASPT2 calculations utilize a full-valence active space, with the MC-PDFT calculation also including two additional oxygen lone-pair orbitals. Additionally, there are results⁶¹ from MC-PDFT and CMS-PDFT²⁶ using a smaller (6,5) active space. This smaller active space was chosen using the ABC2 automatic active-space selection scheme⁷⁶ by setting the parameters A , B , and C to 3, 2, and 0 respectively. We also include results from high-level single-reference methods computed by Budzák *et al.*⁷⁵ including second-order algebraic diagrammatic construction (ADC(2)),⁷⁷ second-order coupled cluster (CC2),⁷⁸ third-order coupled cluster (CC3),^{78,79} and coupled cluster response method with single and double excitations and noniterative connected triple excitations from CC3 (CCSDR(3)).⁸⁰

Relative to the experimental geometry, the L-PDFT ground-state C=O bond length differs by 0.003 Å, the C–H bond length differs by 0.002 Å, and the H–C–H bond angle differs by 0.2° (Table III). For the excited state, the L-PDFT structure has a deviation of 0.005 Å for the C=O bond length, 0.003 Å for the C–H bond length, and 0.5° for the out-of-plane dihedral (η) relative to the experimental geometry (Table III). The L-PDFT

TABLE IV. L-PDFT adiabatic and vertical excitations in eV (not including vibration ZPE) for the first excited state of formaldehyde compared to reported values in the literature.

Method	Basis Set	Adiabatic	Vertical
L-PDFT(12,10)	jun-cc-pVTZ	3.61	3.98
SA-CASSCF(12,12) ³²	aug-cc-pVTZ	3.56	4.04
MC-PDFT(12,12) ³²	aug-cc-pVTZ	3.58	3.92
MC-PDFT(6,5) ⁶¹	jun-cc-pVTZ	3.65	4.07
CMS-PDFT(6,5) ⁶¹	jun-cc-pVTZ	3.65	4.07
CASPT2(12,10) ⁷⁵	aug-cc-pVTZ	3.53	3.92
ADC(2) ⁷⁵	aug-cc-pVTZ		3.92
CCSDR(3) ⁷⁵	aug-cc-pVTZ		3.97
CC3 ^{75,81}	aug-cc-pVTZ	3.58	3.96
expt. ⁸²			3.79

H–C–H bond angle agrees with the experimental value to within 0.1°. L-PDFT has the most accurate η and H–C–H bond angle values of any of the methods presented.

Overall, for predicting the ground- and excited-state structures of formaldehyde, L-PDFT performs similarly to MC-PDFT with the slightly larger (12,12) active space and also similarly to the much more expensive CASPT2 method with the same active space.

Table IV summarizes the adiabatic and vertical excita-

tion energies calculated by L-PDFT and compares them with results from the literature. All values exclude the vibrational ZPE. We take the experimental vertical excitation energy measured by electron-impact spectroscopy as our reference.⁸² It is not possible to compare the adiabatic excitation energy to experiments without the vibrational ZPE. Instead, since the CC3 method is known to get within 0.03 eV of the extrapolated full configuration interaction for a variety of molecules,⁸¹ we take CC3 to be our reference for the adiabatic excitation energy.

Like MC-PDFT, L-PDFT overestimates the vertical excitation energy with a difference of 0.19 eV relative to the experimental value.⁸² However, this should be considered in the context that all methods presented in Table IV deviate by more than 0.1 eV from the experimental vertical excitation energy, which has two kinds of uncertainty. First is the uncertainty due to experimental precision, and second is uncertainty because it is only approximately true that the spectral peak in electron-impact spectroscopy corresponds to a vertical excitation energy. The L-PDFT predicted vertical excitation energy only differs from the CC3 result by 0.02 eV and the much more expensive CASPT2 by 0.06 eV. Additionally, L-PDFT almost exactly reproduces the CC3 adiabatic excitation energy, with a slightly higher excitation energy as compared to CASPT2. Overall, L-PDFT performs similarly to CC3, MC-PDFT, and CASPT2 in predicting both the adiabatic and vertical excitation energies of formaldehyde.

C. *s-trans*-butadiene

Unlike formaldehyde, *s-trans*-butadiene has been shown to have a strong multireference character even in its 1A_g ground state.⁸⁵ Table V summarizes the selected optimized structural parameters of the 1 and 2 1A_g states of *s-trans*-butadiene as calculated by L-PDFT and other multireference methods.³² All active spaces are comprised of four electrons in two π orbitals and two π^* orbitals. Our reference for the ground-state structure is the experimental geometry from Haugen *et al.*⁸⁴, whereas for the excited-state structure we take our prior results calculated at the CASPT2(4,4) level of theory as our reference.³²

In general, L-PDFT performs similarly to both MC-PDFT and CASPT2 at predicting the equilibrium structures. For the ground state, L-PDFT deviates slightly from MC-PDFT for the C–C bond length (difference of 0.007 Å), but still does better than CASPT2 and CC3. Both L-PDFT and MC-PDFT deviate the most from the experimental C=C bond length. For the excited state, L-PDFT and MC-PDFT agree on nearly every parameter except for the C–C bond length where they differ by only 0.002 Å. Overall, L-PDFT performs similarly to MC-PDFT, CASPT2, and CC3 at predicting the ground- and excited-state structures of the challenging *s-trans*-butadiene molecule.

Two very-high-quality estimates of the vertical excitation energy of *s-trans*-butadiene to the 2 1A_g state have been reported in the literature: Watson and Chan⁸⁶ estimated the vertical excitation energy to be 6.39 eV based on extrapolated equation-of-motion coupled-cluster calculations, and Loos *et al.*⁸³ estimated it to be 6.50 eV using an extrapolated complete-basis-set FCI calculation. Multi-state CASPT2⁸⁷ using a (4,4) active space at the equilibrium geometry predicts a vertical excitation of 6.69 eV,⁸⁵ 0.3 eV above the theoretical best estimate (TBE). Table VI summarizes the adiabatic and vertical excitation energies of L-PDFT as compared to the previously computed SA-CASSCF, MC-PDFT, and CASPT2 energies using a two-state model space with a (4,4) active space³² as well as the CC3 vertical . Although the L-PDFT adiabatic excitation energy differs by only 0.1 eV from the CASPT2 predicted adiabatic excitation energy and by only 0.01 eV from MC-PDFT, it overestimates the vertical excitation energy by more than 0.4 eV as compared to the best available estimates.

D. Phenol

The photochemistry of phenol has been extensively studied as it is a prototype of the $^1\pi\sigma^*$ motif which is common in a variety of biomolecules and aromatic compounds.^{12,88–95} In the original L-PDFT paper, we studied the O–H photodissociation potential energy surface and found that L-PDFT was able to correctly model the potential energy surface near the conical intersection, whereas MC-PDFT surfaces unphysically crossed.²⁷ Our active space in this paper is the same as in our prior studies of phenol^{26,27,61} consisting of $3(\pi, \pi^*)$, the p_z of O, and the C–O and O–H σ and σ^* orbitals.

Selected L-PDFT optimized ground- and first excited-state internal coordinates of phenol are presented in Table VII and are compared with results from other, similar methods. Our reference for the ground- and excited-state geometries are the experimental structures determined by Larsen⁹⁶ and Spangenberg *et al.*⁹⁷ respectively. All of the PDFT and CASSCF methods in Table VII use the same (12,11) active space. We also include results from a high-level semiempirical fit that was designed to replicate the ZPE-inclusive experimental adiabatic excitation energy.⁹³ All of the methods in the table predict relatively similar ground-state geometries, in line with the experimentally determined geometry.⁹⁶ Of interest is that the excited-state geometry optimized with MC-PDFT is nonplanar, with a substantial C–C–O–H dihedral of 14.3°.⁶¹ It was noted that CMS-PDFT does not suffer from this incorrect nonplanarity because it correctly incorporates the state interaction between S_0 and S_1 . L-PDFT also correctly predicts a planar excited-state geometry, in agreement with CMS-PDFT⁶¹ and experimental results.⁹⁷ This confirms that L-PDFT accounts for the state interaction as well as CMS-PDFT does. Overall, L-PDFT performs better than MC-PDFT

TABLE V. Selected L-PDFT optimized internal coordinates for the ground and excited 1A_g states of *s-trans*-butadiene as compared to results from other methods. All bond lengths are in Å and all bond angles are in degrees. Experimental uncertainty shown in parentheses.

State	Method	Basis Set	$r_{C=C}$	r_{CC}	θ_{CCC}
$1\ {}^1A_g$	L-PDFT(4,4)	jul-cc-pVTZ	1.335	1.460	124.1
	SA-CASSCF(4,4) ³²	aug-cc-pVTZ	1.345	1.456	124.3
	MC-PDFT(4,4) ³²	aug-cc-pVTZ	1.336	1.470	124.1
	CASPT2(4,4) ³²	aug-cc-pVTZ	1.342	1.454	123.6
	CC3 ⁸³	aug-cc-pVTZ	1.340	1.453	123.9
	expt. ⁸⁴		1.343(1)	1.467(1)	122.8(5)
$2\ {}^1A_g$	L-PDFT(4,4)	jul-cc-pVTZ	1.496	1.399	124.1
	SA-CASSCF(4,4) ³²	aug-cc-pVTZ	1.489	1.413	123.2
	MC-PDFT(4,4) ³²	aug-cc-pVTZ	1.496	1.397	124.1
	CASPT2(4,4) ³²	aug-cc-pVTZ	1.488	1.394	122.1

TABLE VI. L-PDFT adiabatic and vertical excitations in eV (not including vibrational ZPE) for the $2\ {}^1A_g$ state of *s-trans*-butadiene compared to reported values in the literature.

Method	Basis Set	Adiabatic	Vertical
L-PDFT(4,4)	jul-cc-pVTZ	5.78	6.92
SA-CASSCF(4,4) ³²	aug-cc-pVTZ	5.42	6.57
MC-PDFT(4,4) ³²	aug-cc-pVTZ	5.77	6.91
CASPT2(4,4) ³²	aug-cc-pVTZ	5.68	6.68
CCSD ^{a85}	6-31G**		7.69
MS-CASPT2(4,4) ^{a85}	6-31G**		6.69
CC3 ⁸³	aug-cc-pVTZ		6.67
Watson and Chan ⁸⁶ TBE ^b			6.39
Loos <i>et al.</i> ⁸³ TBE ^b			6.50

^a Excitation energy calculated at experimental equilibrium geometry.

^b Theoretical best estimate.

in accurately predicting the first excited-state geometry of phenol, and the results are similar to those for CMS-PDFT and other high-level methods.

Table VIII contains a summary of the vertical and adiabatic excitation energies of phenol as obtained by L-PDFT and other methods. As in our previous work,⁶¹ we take as our reference the high-level semiempirical fit by Zhu *et al.*⁹³ for both excitation energies. We also include results from CC2¹⁰⁰ (for which the ground-state geometries are optimized at the second-order Møller-Plesset perturbation theory (MP2)^{105,106}), internally contracted multireference configuration interaction (MRCI)¹⁰⁷ based on a CASSCF(10,9) wave function,¹⁰¹ and CASPT2 using a (8,8)⁹⁸ and (10,10)⁹⁹ active space. Both the MRCI and CASPT2 results were computed at their respective reference CASSCF optimized geometries.

L-PDFT performs similarly to the previously reported MC-PDFT results⁶¹ and overestimates the vertical and adiabatic excitation energy relative to the reference by about 0.2 eV. Comparatively, CASPT2 using both an (8,8)⁹⁸ and (10,10)⁹⁹ active space underestimates the

vertical and adiabatic excitation energy by more than 0.2 eV. The relative difference between the L-PDFT vertical and adiabatic excitation energies is 0.18 eV which is similar to the relative difference of 0.17 eV predicted by the semiempirical fit.⁹³

E. Cytosine

Finally, we report the optimized ground- and excited-state geometries and the adiabatic and vertical excitation energies of the nucleobase cytosine (Fig. 3). Previous studies have shown that the (14,10) active space composed of five π , two lone-pair, and three π^* orbitals is sufficient for studying the low-lying excited states of cytosine.^{108–110}

For the ground state, we take the experimental structure determined by Barker and Marsh¹⁰³ as our reference. Tables IX and X contain selected optimized bond lengths and angles respectively obtained from L-PDFT and other methods. All methods presented in Table IX perform similarly with a mean unsigned deviation (MUD) of 0.02 Å relative to the experimental bond lengths. L-PDFT performs identically to MC-PDFT for determining the cytosine bond angles with an MUD of 1.6° for both methods.

Due to the lack of experimental data for the $2\ {}^1A'$ relaxed geometry, we take the MS-CASPT2 with an (8,7) active space from the study by Nakayama *et al.*¹⁰⁴ as our reference. Tables XI and XII compares the same selected $2\ {}^1A'$ optimized bond lengths and bond angles for L-PDFT and other methods. All methods give similar optimized bond lengths for the excited state with L-PDFT and MC-PDFT both having a MUD of 0.02 Å. CASPT2 and SA-CASSCF have relatively larger MUDs of 0.04 Å and 0.05 Å respectively. L-PDFT and MC-PDFT predict similar bond angles of the excited state, with L-PDFT being slightly closer to the MS-CASPT2 results with a MUD of 1.1°. CASPT2 has the widest difference in the bond angles, and it overestimates the 7-5-6 bond angle

TABLE VII. L-PDFT selected internal coordinates for the ground- and first excited-state of phenol compared with various methods. All bond lengths are in Å and all angles are in degrees. The experimental uncertainty is shown in parentheses.

State	Method	Basis Set	Avg. r_{CC}	r_{CO}	r_{OH}	θ_{COH}	τ_{CCOH}
S_0	L-PDFT(12,11)	jul-cc-pVDZ	1.400	1.369	0.962	109.4	0.0
	SA-CASSCF(12,11) ⁶¹	jul-cc-pVDZ	1.399	1.384	0.966	109.3	0.0
	MC-PDFT(12,11) ⁶¹	jul-cc-pVDZ	1.401	1.370	0.964	109.2	0.0
	CMS-PDFT(12,11) ⁶¹	jul-cc-pVDZ	1.398	1.367	0.966	109.2	0.0
	semiemp. fit ⁹³		1.395	1.382	0.965	108.5	0.0
	expt. ⁹⁶		1.393	1.375(5)	0.957(6)	108.8(4)	0.0
S_1	L-PDFT(12,11)	jul-cc-pVDZ	1.431	1.346	0.964	109.4	0.0
	SA-CASSCF(12,11) ⁶¹	jul-cc-pVDZ	1.434	1.379	0.960	109.3	0.0
	MC-PDFT(12,11) ⁶¹	jul-cc-pVDZ	1.429	1.337	0.975	108.2	14.3
	CMS-PDFT(12,11) ⁶¹	jul-cc-pVDZ	1.435	1.362	0.962	109.2	0.0
	semiemp. fit ⁹³		1.427	1.367	0.963	108.7	0.0
	expt. ⁹⁷		1.423	1.356	0.992	108.8	0.0

TABLE VIII. L-PDFT adiabatic and vertical excitations in eV (not including vibration ZPE) for the first excited state of phenol compared to reported values in the literature.

Method	Basis Set	Adiabatic	Vertical
L-PDFT(12,11)	jul-cc-pVDZ	4.85	5.03
SA-CASSCF(12,11) ⁶¹	jul-cc-pVDZ	4.73	4.93
MC-PDFT(12,11) ⁶¹	jul-cc-pVDZ	4.83	5.03
CMS-PDFT(12,11) ⁶¹	jul-cc-pVDZ	4.72	4.93
CASPT2(8,8) ^{a98}	cc-pVDZ	4.36	4.64
CASPT2(10,10) ^{a99}	aug(O)-AVTZ ^b	4.37	4.52
CC2 ^{c100}	aug-cc-pVDZ	4.67	4.86
MRCI(10,9) ^{ad101}	aug-cc-pVDZ	4.82	4.75
semiemp. fit ⁹³		4.66	4.83

^a Excitations calculated at the CASSCF optimized geometry.

^b Modified aug-cc-pVTZ basis set with extra even tempered sets of s and p diffuse functions on the oxygen atom.

^c Ground state optimized with MP2 and excited state optimized with CC2.

^d It is possible for the vertical excitation to be lower than the adiabatic excitation when the excitations are computed at geometries optimized at a different level of theory.

by about 7° as compared to all of the other methods.

Table XIII summarizes the adiabatic and vertical excitation energies for the 2 ¹A' state of cytosine computed at various levels of theory. We take the experimental vertical excitation from Abouaf *et al.*¹¹², and the MS-CASPT2(12,9) result (ground-state geometry optimized with MP2 and excited-state geometry optimized with MS-CASPT2(8,7)) as the reference for the adiabatic excitation energy Nakayama *et al.*¹⁰⁴. All methods, except CC2, perform similarly with L-PDFT underestimating the reference vertical excitation energy the most. CC2 gets the closest to the experimental vertical excitation energy, differing only by 0.11 eV. Both L-PDFT and MC-PDFT get within 0.1 eV of the MS-CASPT2 adiabatic excitation energy. Overall, L-PDFT differs from MC-PDFT by only 0.03 eV for both the adiabatic and

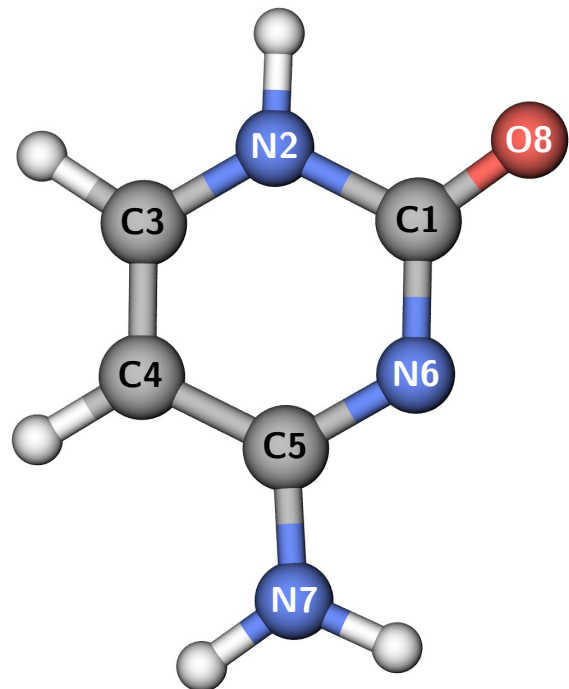


FIG. 3. Ground-state geometry of cytosine optimized with L-PDFT.

vertical excitation energies.

V. CONCLUSION

We presented the derivation and implementation of analytic nuclear gradients for L-PDFT calculations based on SA-CASSCF wave functions. Because the final L-PDFT wave function is not fully variational with respect to all its parameters, we used a Lagrangian method similar to that used previously for SA-CASSCF and MC-PDFT analytic gradients. As in SA-CASSCF, we as-

TABLE IX. Selected L-PDFT ground state cytosine bond lengths (in Å) compared with similar methods and experimental quantities. Atoms are labeled according to Fig. 3.

Method	Basis Set	C1-N2	N2-C3	C3-C4	C4-C5	C5-N7	C5-N6	N6-C1	C1-O8	MUD ^a
L-PDFT(14,10)	jul-cc-pVTZ	1.438	1.344	1.361	1.434	1.352	1.327	1.363	1.218	0.02
SA-CASSCF(14,10) ³²	aug-cc-pVTZ	1.391	1.354	1.346	1.446	1.350	1.291	1.391	1.296	0.02
MC-PDFT(14,10) ³²	aug-cc-pVTZ	1.440	1.340	1.358	1.436	1.351	1.326	1.364	1.215	0.02
CCSD ¹⁰²	TZP	1.416	1.360	1.353	1.446	1.357	1.313	1.379	1.214	0.02
CASPT2(14,10) ³²	6-311G+(2df)	1.420	1.362	1.357	1.443	1.360	1.320	1.378	1.222	0.02
expt. ¹⁰³		1.374	1.357	1.342	1.424	1.330	1.337	1.364	1.234	

^a Mean unsigned deviation from experiment.

TABLE X. Selected L-PDFT ground state cytosine bond angles (in degrees) compared with similar methods and experimental quantities. Atoms are labeled according to Fig. 3.

Method ^a	θ_{6-1-2}	θ_{5-6-1}	θ_{4-5-6}	θ_{3-2-1}	θ_{3-4-5}	θ_{4-3-2}	θ_{8-1-2}	θ_{8-1-6}	θ_{7-5-6}	θ_{7-5-4}	MUD ^b
L-PDFT(14,10)	116.0	120.4	124.2	123.2	115.8	120.4	117.3	126.6	116.2	119.6	1.6
SA-CASSCF(14,10) ³²	119.3	119.3	120.6	122.3	118.4	120.3	120.0	120.8	118.0	121.7	0.9
MC-PDFT(14,10) ³²	115.8	120.5	124.0	123.4	115.7	119.6	117.5	117.7	116.4	119.5	1.6
CCSD ¹⁰²	119.7	120.1	119.5	121.9	118.8	120.2	120.9	119.6	119.2	121.5	1.3
CASPT2(14,10) ³²	119.9	120.1	119.3	121.7	118.9	120.3	120.9	119.4	119.5	121.4	1.4
expt. ¹⁰³	119.1	119.9	122.0	122.7	117.3	120.1	119.8	122.2	118.2	119.9	

^a Methods are the same as in Table IX.

^b Mean unsigned deviation from experiment.

summed equal weights to exclude the model states from the response equations. We then implemented the gradients in PYSCF-FORGE, which is a library of PYSCF extensions, and we showed that they agree with numerical gradients for both HeH⁺ and LiH using both translated and fully-translated functionals. We showed the utility of the L-PDFT analytic gradients by optimizing the ground and first excited singlet states of formaldehyde, *s-trans*-butadiene, phenol, and the nucleobase cytosine. Whereas MC-PDFT predicts a nonplanar first excited state of phenol, we showed that L-PDFT correctly predicts a planar structure. Additionally, we computed the vertical and adiabatic excitation energy for each molecule and saw that L-PDFT performs similarly for excitation energies to MC-PDFT and other high-level multireference methods like CASPT2.

These results are consistent with our prior study and benchmarking of L-PDFT for calculating vertical excitation energies and for modeling potential energy surfaces.^{27,29} Specifically, L-PDFT correctly models the potential energy surfaces near conical intersections and locally avoided crossings whereas MC-PDFT is inaccurate.²⁷ The results are especially encouraging because of the low cost of L-PDFT relative to MS-CASPT2 and MRCI. We conclude that L-PDFT is promising new tool for studying excited-state geometries, both vertical and adiabatic energies, photochemical reactions, and electronically nonadiabatic dynamics.

SUPPLEMENTARY MATERIAL

See the supplementary material associated with this article for the analytic and numerical gradients of HeH⁺ and LiH at each geometry and L-PDFT optimized structures with their corresponding energies.

ACKNOWLEDGMENTS

This work was supported in part by the National Science Foundation under Grant No. CHE-2054723. M.R. Hennefarth acknowledges support by the National Science Foundation Graduate Research Fellowship under Grant No. 2140001. We also acknowledge the University of Chicago’s Research Computing Center for their support of this work. Any opinion, findings, and conclusions or recommendations expressed in this material are those of the author(s) and do not necessarily reflect the views of the National Science Foundation.

Appendix A: The Translated and Fully-Translated On-Top Functionals

Current generation on-top functionals include translated¹⁹ or fully-translated⁴⁴ KS local-spin density approximations or generalized gradient approximations functionals. These on-top functionals are defined such that

$$E^{\text{ot}}[\vec{\rho}] = E^{\text{xc}}[\vec{\rho}] \quad (\text{A1})$$

TABLE XI. Selected L-PDFT $2^1A'$ excited state cytosine bond lengths (in Å) compared with similar methods and experimental quantities. Atoms are labeled according to Fig. 3.

Method	Basis Set	C1-N2	N2-C3	C3-C4	C4-C5	C5-N7	C5-N6	N6-C1	C1-O8	MUD ^a
L-PDFT(14,10)	jul-cc-pVTZ	1.398	1.390	1.415	1.376	1.361	1.406	1.313	1.271	0.02
SA-CASSCF(14,10) ³²	aug-cc-pVTZ	1.358	1.381	1.424	1.365	1.372	1.417	1.274	1.328	0.04
MC-PDFT(14,10) ³²	aug-cc-pVTZ	1.429	1.382	1.416	1.385	1.369	1.416	1.342	1.236	0.02
CASPT2(14,10) ³²	6-311G+(2df)	1.453	1.301	1.394	1.444	1.350	1.320	1.374	1.210	0.05
MS-CASPT2(8,7) ¹⁰⁴	Sapporo-DZP	1.410	1.376	1.430	1.391	1.397	1.351	1.325	1.276	

^a Mean unsigned deviation from MS-CASPT2.

TABLE XII. Selected L-PDFT $2^1A'$ excited state cytosine bond angles (in degrees) compared with similar methods and experimental quantities. Atoms are labeled according to Fig. 3.

Method ^a	θ_{6-1-2}	θ_{5-6-1}	θ_{4-5-6}	θ_{3-2-1}	θ_{3-4-5}	θ_{4-3-2}	θ_{8-1-2}	θ_{8-1-6}	θ_{7-5-6}	θ_{7-5-4}	MUD ^b
L-PDFT(14,10)	122.7	117.1	122.6	121.7	119.9	115.9	114.1	123.2	111.9	125.5	1.1
SA-CASSCF(14,10) ³²	126.6	116.1	121.6	119.8	119.6	116.4	112.1	121.2	112.7	125.8	1.6
MC-PDFT(14,10) ³²	121.4	118.1	121.7	121.1	120.4	117.4	115.7	122.9	112.2	126.2	1.9
CASPT2(14,10) ³²	118.1	119.1	122.8	123.4	118.4	118.3	116.7	125.2	119.0	118.3	3.0
MS-CASPT2(8,7) ¹⁰⁴	123.0	115.8	123.4	122.7	119.6	115.4	111.8	125.2	112.8	123.7	

^a Methods are the same as in Table XI.

^b Mean unsigned deviation from MS-CASPT2.

TABLE XIII. L-PDFT adiabatic and vertical excitations in eV (not including vibration ZPE) for the $2^1A'$ state of cytosine compared to reported values in the literature.

Method	Basis Set	Adiabatic	Vertical
L-PDFT(14,10)	jul-cc-pVTZ	4.05	4.42
MC-PDFT(14,10) ³²	aug-cc-pVTZ	4.08	4.45
CC2 ¹¹¹	aug-cc-pVDZ		4.54
MS-CASPT2(12,9) ^{a104}	Sapporo-DZP	3.98	4.48
expt. ¹¹²			4.65

^a Ground-state geometry optimized with MP2 and excited-state geometry optimized with MS-CASPT2(8,7).

where E^{xc} is a KS exchange-correlation functional and $\vec{\rho}$ are the collective translated (or fully-translated) spin-density variables and their gradients.

$$\vec{\rho}^T = [\rho_{\uparrow} \ \rho_{\downarrow} \ \sigma_{\uparrow\uparrow} \ \sigma_{\uparrow\downarrow} \ \sigma_{\downarrow\downarrow}] \quad (\text{A2})$$

Here, ρ_{\uparrow} and ρ_{\downarrow} are effective spin densities, with primes denoting the gradient with respect to electron coordinate; and $\sigma_{\uparrow\uparrow}$, $\sigma_{\uparrow\downarrow}$, and $\sigma_{\downarrow\downarrow}$ being the inner product of the effective spin density gradients.

$$\sigma_{\uparrow\uparrow} = \rho'_{\uparrow} \cdot \rho'_{\uparrow} \quad (\text{A3a})$$

$$\sigma_{\uparrow\downarrow} = \rho'_{\uparrow} \cdot \rho'_{\downarrow} \quad (\text{A3b})$$

$$\sigma_{\downarrow\downarrow} = \rho'_{\downarrow} \cdot \rho'_{\downarrow} \quad (\text{A3c})$$

For translated functionals, the following mapping is used to generate the effective spin densities and their gradients from the wave function's density and on-top pair density:

$$\rho_{\uparrow} = \frac{\rho}{2}(1 + \zeta_t) \quad (\text{A4})$$

$$\rho_{\downarrow} = \frac{\rho}{2}(1 - \zeta_t) \quad (\text{A5})$$

$$\rho'_{\uparrow} = \frac{\rho'}{2}(1 + \zeta_t) \quad (\text{A6})$$

$$\rho'_{\downarrow} = \frac{\rho'}{2}(1 - \zeta_t) \quad (\text{A7})$$

where ζ_t is given by

$$\zeta_t = \begin{cases} \sqrt{1-R} & R \leq 1 \\ 0 & R > 1 \end{cases} \quad (\text{A8})$$

and R is proportional to the ratio of the on-top density to the density.

$$R = \frac{4\Pi}{\rho^2} \quad (\text{A9})$$

Both ζ_t and R are functions of \mathbf{r} . Functionals translated by this scheme are simply known as 'translated' functionals and are given the prefix 't'.¹⁹

The above translation scheme has a discontinuity in its first derivative at $R = 1$. The fully-translated scheme⁴⁴ fixes this by using a polynomial interpolation to smooth out the discontinuity in the region of R close to 1 as

$$\rho_{\uparrow} = \frac{\rho}{2}(1 + \zeta_{ft}) \quad (\text{A10})$$

$$\rho_{\downarrow} = \frac{\rho}{2}(1 - \zeta_{ft}) \quad (\text{A11})$$

TABLE XIV. Parameter values for the fully-translated scheme.

Parameter	Value
R_0	0.9
R_1	1.15
A	-475.606 560 09
B	-379.473 319 22
C	-85.381 496 82

$$\rho'_\uparrow = \frac{\rho'}{2}(1 + \zeta_{\text{ft}}) + \frac{\rho}{2}\zeta'_{\text{ft}} \quad (\text{A12})$$

$$\rho'_\downarrow = \frac{\rho'}{2}(1 - \zeta_{\text{ft}}) - \frac{\rho}{2}\zeta'_{\text{ft}} \quad (\text{A13})$$

where ζ_{ft} is

$$\zeta_{\text{ft}} = \begin{cases} \sqrt{1-R} & R < R_0 \\ P(R) & R_0 \leq R \leq R_1 \\ 0 & R > R_1 \end{cases} \quad (\text{A14})$$

and P is the polynomial interpolation from R_0 to R_1 .

$$P = P(R) = A(R - R_1)^5 + B(R - R_1)^4 + C(R - R_1)^3 \quad (\text{A15})$$

The gradient of ζ_{ft} is given by

$$\zeta'_{\text{ft}} = \begin{cases} -\frac{R'}{2\zeta_{\text{ft}}} & R < R_0 \\ R'P^{(1)} & R_0 \leq R \leq R_1 \\ 0 & R > R_1 \end{cases} \quad (\text{A16})$$

where R' is written as

$$R' = \frac{4\Pi'}{\rho^2} - \frac{8\Pi\rho'}{\rho^3} = R\left(\frac{\Pi'}{\Pi} - \frac{2\rho'}{\rho}\right) \quad (\text{A17})$$

and $P^{(1)}$ is the first derivative of P with respect to R .

$$P^{(1)} = 5A(R - R_1)^4 + 4B(R - R_1)^3 + 3C(R - R_1)^2 \quad (\text{A18})$$

The parameters A, B, C, R_0 , and R_1 are given in Table XIV

ζ_t can be considered a special case of ζ_{ft} with $R_0 = R_1 = 1$. Then, ζ can be used to denote either ζ_t or ζ_{ft} with it being clear from the context which form is being used. Consequently, the main difference between translated and fully-translated functionals is the form of ρ'_\uparrow and ρ'_\downarrow .

Appendix B: SA-CASSCF Hessian in the L-PDFT Eigenstate Basis

The CI portion of the SA-CASSCF Hessian matrix, $\mathbf{H}_{\mathbf{P}_\perp \mathbf{P}_\perp}^{E^{\text{SA}}}$, can be expressed either in the SA-CASSCF or L-PDFT eigenstate basis. We define Θ_{IJ}^{MN} and $\tilde{\Theta}_{\Lambda\Gamma}^{MN}$ as

the elements of the CI Hessian in the SA-CASSCF and L-PDFT eigenstate bases respectively.

$$\Theta_{IJ}^{MN} = \frac{\partial^2 E^{\text{SA}}}{\partial P_M^I \partial P_N^J} \quad (\text{B1})$$

$$\tilde{\Theta}_{\Lambda\Gamma}^{MN} = \frac{\partial^2 E^{\text{SA}}}{\partial P_M^\Lambda \partial P_N^\Gamma} \quad (\text{B2})$$

From Eq. 30 of Ref. 30, the elements of $\mathbf{H}_{\mathbf{P}_\perp \mathbf{P}_\perp}^{E^{\text{SA}}}$ in the SA-CASSCF eigenstate basis can be written as

$$\Theta_{IJ}^{MN} = \frac{2\delta_{IJ}}{n^{\text{SA}}} \langle M | (\hat{H}^{\text{el}} - E_I^{\text{CAS}}) | N \rangle \quad (\text{B3})$$

where n^{SA} are the number of states in the model space, \hat{H}^{el} is the real electronic Hamiltonian, and E_I^{CAS} is the CASSCF energy for state $|I\rangle$.

In our implementation, we evaluate $\mathbf{H}_{\mathbf{P}_\perp \mathbf{P}_\perp}^{E^{\text{SA}}}$ in the L-PDFT eigenstate basis. The matrices Θ^{MN} and $\tilde{\Theta}^{MN}$ are related to one another by the transformation matrix \mathbf{U} that rotates the SA-CASSCF states into the L-PDFT states.

$$\tilde{\Theta}^{MN} = \mathbf{U}^\top \Theta^{MN} \mathbf{U} \quad (\text{B4})$$

The matrix \mathbf{U} is determined by diagonalizing the projected L-PDFT Hamiltonian in the SA-CASSCF eigenstate basis (Eq. 16). Hence, we have that

$$\frac{\partial^2 E^{\text{SA}}}{\partial P_M^\Lambda \partial P_N^\Gamma} = \frac{2}{n^{\text{SA}}} \langle M | (\delta_{\Gamma\Lambda} \hat{H}^{\text{el}} - E_I^{\text{CAS}} U_\Gamma^I U_\Lambda^I) | N \rangle \quad (\text{B5})$$

where U_Γ^I are elements of the matrix \mathbf{U} . Note that $E_I^{\text{CAS}} U_\Gamma^I U_\Lambda^I$ contains off-diagonal elements that most implementations of the SA-CASSCF Hessian matrix, which usually presume evaluation in the SA-CASSCF eigenstate basis, would omit.

Appendix C: On-Top Gradient

The first derivative of the on-top kernel (ϵ^{xc}) with respect to the density variables $\vec{\rho}$ (\mathbf{v}^{ot}) is obtained using the chain-rule

$$\mathbf{v}^{\text{ot}} = \mathbf{v}^{\text{xc}} \cdot \mathbf{J}_{\vec{\rho}}^{\vec{\rho}} \quad (\text{C1})$$

where \mathbf{v}^{xc} is described by

$$\mathbf{v}^{\text{xc}} = \nabla_{\vec{\rho}} \epsilon^{\text{xc}} = \left[\frac{\partial \epsilon^{\text{xc}}}{\partial \rho_\uparrow} \quad \frac{\partial \epsilon^{\text{xc}}}{\partial \rho_\downarrow} \quad \frac{\partial \epsilon^{\text{xc}}}{\partial \sigma_{\uparrow\uparrow}} \quad \frac{\partial \epsilon^{\text{xc}}}{\partial \sigma_{\uparrow\downarrow}} \quad \frac{\partial \epsilon^{\text{xc}}}{\partial \sigma_{\downarrow\downarrow}} \right] \quad (\text{C2})$$

$$\mathbf{J}_{\vec{\rho}}^{\vec{\rho}} = \begin{bmatrix} \frac{\partial \rho_\uparrow}{\partial \rho} & \frac{\partial \rho_\uparrow}{\partial \Pi} & \frac{\partial \rho_\uparrow}{\partial \rho'} & \frac{\partial \rho_\uparrow}{\partial \Pi'} \\ \frac{\partial \rho_\downarrow}{\partial \rho} & \frac{\partial \rho_\downarrow}{\partial \Pi} & \frac{\partial \rho_\downarrow}{\partial \rho'} & \frac{\partial \rho_\downarrow}{\partial \Pi'} \\ \frac{\partial \sigma_{\uparrow\uparrow}}{\partial \rho} & \frac{\partial \sigma_{\uparrow\uparrow}}{\partial \Pi} & \frac{\partial \sigma_{\uparrow\uparrow}}{\partial \rho'} & \frac{\partial \sigma_{\uparrow\uparrow}}{\partial \Pi'} \\ \frac{\partial \sigma_{\uparrow\downarrow}}{\partial \rho} & \frac{\partial \sigma_{\uparrow\downarrow}}{\partial \Pi} & \frac{\partial \sigma_{\uparrow\downarrow}}{\partial \rho'} & \frac{\partial \sigma_{\uparrow\downarrow}}{\partial \Pi'} \\ \frac{\partial \sigma_{\downarrow\downarrow}}{\partial \rho} & \frac{\partial \sigma_{\downarrow\downarrow}}{\partial \Pi} & \frac{\partial \sigma_{\downarrow\downarrow}}{\partial \rho'} & \frac{\partial \sigma_{\downarrow\downarrow}}{\partial \Pi'} \end{bmatrix} \quad (\text{C3})$$

and $\mathbf{J}_{\vec{\rho}}^{\vec{\rho}}$ is the Jacobian matrix for the translation scheme (which has been derived previously).^{31,32}

$$\mathbf{f}^{\text{ot}} = \left(\mathbf{J}_{\vec{\rho}}^{\rho\Pi} \right)^\top \cdot \mathbf{f}^{\rho\Pi} \cdot \mathbf{J}_{\vec{\rho}}^{\rho\Pi} + \mathbf{v}^{\rho\Pi} \cdot \mathbf{H}_{\vec{\rho}}^{\rho\Pi} \quad (\text{D13})$$

and the gradients are related by

$$\mathbf{v}^{\rho m} = \mathbf{v}^{\text{xc}} \cdot \mathbf{J}_{\rho m}^{\uparrow\downarrow} \quad (\text{D14})$$

$$\mathbf{v}^{\rho\zeta} = \mathbf{v}^{\rho m} \cdot \mathbf{J}_{\rho\zeta}^{\rho m} \quad (\text{D15})$$

$$\mathbf{v}^{\rho R} = \mathbf{v}^{\rho\zeta} \cdot \mathbf{J}_{\rho R}^{\rho\zeta} \quad (\text{D16})$$

$$\mathbf{v}^{\rho\Pi} = \mathbf{v}^{\rho\Pi} \cdot \mathbf{J}_{\rho\Pi}^{\rho\Pi} \quad (\text{D17})$$

All Jacobians and Hessians used for the translated functionals will be prefixed with a ‘t’ (for example, ${}^t\mathbf{J}$ and ${}^t\mathbf{H}$), and Jacobians and Hessians used for fully-translated functionals will be prefixed with an ‘ft’ (for example, ${}^{\text{ft}}\mathbf{J}$ and ${}^{\text{ft}}\mathbf{H}$). Once we arrive at the coordinates of (ρ, Π) , we can then change the variables to $\vec{\rho}$, which will be the same for translated and fully-translated functionals.

1. Translated On-Top Hessian

We now go to the variables (ρ, ζ) by

$$\begin{bmatrix} \rho \\ m \\ \sigma_{\rho\rho} \\ \sigma_{\rho m} \\ \sigma_{mm} \end{bmatrix} = \begin{bmatrix} \rho \\ \rho\zeta \\ \sigma_{\rho\rho} \\ \zeta\sigma_{\rho\rho} \\ \zeta^2\sigma_{\rho\rho} \end{bmatrix} \quad (\text{D18})$$

Then

$${}^t\mathbf{J}_{\rho\zeta}^{\rho m} = \begin{bmatrix} 1 & 0 & 0 & 0 & 0 \\ \zeta & \rho & 0 & 0 & 0 \\ 0 & 0 & 1 & 0 & 0 \\ 0 & \sigma_{\rho\rho} & \zeta & 0 & 0 \\ 0 & 2\zeta\sigma_{\rho\rho} & \zeta^2 & 0 & 0 \end{bmatrix} \quad (\text{D19})$$

$$\mathbf{v}^{\rho m} \cdot {}^t\mathbf{H}_{\rho\zeta}^{\rho m} = \begin{bmatrix} 0 \\ \epsilon_m^{\text{ot}} & 2\epsilon_{\sigma_{mm}}^{\text{ot}} \sigma_{\rho\rho} \\ 0 & \epsilon_{\sigma_{\rho m}}^{\text{ot}} + 2\epsilon_{\sigma_{mm}}^{\text{ot}} \zeta & 0 \\ 0 & 0 & 0 & 0 \\ 0 & 0 & 0 & 0 & 0 \end{bmatrix} \quad (\text{D20})$$

Our next transformation is to (ρ, R) using

$$\begin{bmatrix} \rho \\ \zeta \\ \sigma_{\rho\rho} \\ \sigma_{\rho\zeta} \\ \sigma_{\zeta\zeta} \end{bmatrix} = \begin{bmatrix} \rho \\ f(R) \\ \sigma_{\rho\rho} \\ 0 \\ 0 \end{bmatrix} \quad (\text{D21})$$

Note that in the translated case, there is no dependence on ζ' ; therefore, the $\sigma_{\rho\zeta}$ and $\sigma_{\zeta\zeta}$ components do not contribute. Here, we are treating $f(R) = f$ and a general

function of R where $f' = \frac{df}{dR}$. Our Jacobian and Hessian for this step are

$${}^t\mathbf{J}_{\rho R}^{\rho\zeta} = \begin{bmatrix} 1 & 0 & 0 & 0 & 0 \\ 0 & f' & 0 & 0 & 0 \\ 0 & 0 & 1 & 0 & 0 \\ 0 & 0 & 0 & 0 & 0 \\ 0 & 0 & 0 & 0 & 0 \end{bmatrix} \quad (\text{D22})$$

$$\mathbf{v}^{\rho\zeta} \cdot {}^t\mathbf{H}_{\rho R}^{\rho\zeta} = \begin{bmatrix} 0 \\ 0 & \epsilon_{\zeta}^{\text{ot}} f'' \\ 0 & 0 & 0 \\ 0 & 0 & 0 & 0 \\ 0 & 0 & 0 & 0 & 0 \end{bmatrix} \quad (\text{D23})$$

where f'' is the second derivative of ζ with respect to R .

Next we go to the (ρ, Π) variables by the following transformation:

$$\begin{bmatrix} \rho \\ R \\ \sigma_{\rho\rho} \\ \sigma_{\rho R} \\ \sigma_{RR} \end{bmatrix} = \begin{bmatrix} \rho \\ \frac{4\Pi}{\rho^2} \\ \sigma_{\rho\rho} \\ 0 \\ 0 \end{bmatrix} \quad (\text{D24})$$

Again, we can omit the $\sigma_{\rho R}$ and σ_{RR} variables since translated functionals do not depend on R' . This transformation results in

$${}^t\mathbf{J}_{\rho\Pi}^{\rho R} = \frac{4}{\rho^2} \begin{bmatrix} 1 & 0 & 0 & 0 & 0 \\ \frac{-2\Pi}{\rho} & 1 & 0 & 0 & 0 \\ 0 & 0 & 1 & 0 & 0 \\ 0 & 0 & 0 & 0 & 0 \\ 0 & 0 & 0 & 0 & 0 \end{bmatrix} \quad (\text{D25})$$

$$\mathbf{v}^{\rho R} \cdot {}^t\mathbf{H}_{\rho\Pi}^{\rho R} = \frac{2\epsilon_R^{\text{ot}}}{\rho^2} \begin{bmatrix} 3R \\ \frac{-4}{\rho} & 0 \\ 0 & 0 & 0 \\ 0 & 0 & 0 & 0 \\ 0 & 0 & 0 & 0 & 0 \end{bmatrix} \quad (\text{D26})$$

2. Fully-Translated On-Top Hessian

For the fully-translated case, going to the (ρ, m) variables modifies $\sigma_{\rho m}$ and σ_{mm} in Eq. D18 such that

$$\begin{bmatrix} \rho \\ m \\ \sigma_{\rho\rho} \\ \sigma_{\rho m} \\ \sigma_{mm} \end{bmatrix} = \begin{bmatrix} \rho \\ \rho\zeta \\ \sigma_{\rho\rho} \\ \zeta\sigma_{\rho\rho} + \rho\sigma_{\rho\zeta} \\ \zeta^2\sigma_{\rho\rho} + 2\rho\zeta\sigma_{\rho\zeta} + \rho^2\sigma_{\zeta\zeta} \end{bmatrix} \quad (\text{D27})$$

The fully-translated Jacobian and Hessian for this translation step are slight modifications of the translated matrices.

$${}^{\text{ft}}\mathbf{J}_{\rho\zeta}^{\rho m} = {}^t\mathbf{J}_{\rho\zeta}^{\rho m} + \tilde{\mathbf{J}}_{\rho\zeta}^{\rho m} \quad (\text{D28})$$

$$\tilde{\mathbf{J}}_{\rho\zeta}^{\rho m} = \begin{bmatrix} 0 & 0 & 0 & 0 & 0 \\ 0 & 0 & 0 & 0 & 0 \\ 0 & 0 & 0 & 0 & 0 \\ \sigma_{\rho\zeta} & 0 & 0 & \rho & 0 \\ 2(\rho\sigma_{\zeta\zeta} + \zeta\sigma_{\rho\zeta}) & 2\rho\sigma_{\rho\zeta} & 0 & 2\rho\zeta & \rho^2 \end{bmatrix} \quad (\text{D29})$$

$$\mathbf{v}^{\rho m} \cdot {}^{\text{ft}}\mathbf{H}_{\rho\zeta}^{\rho m} = \mathbf{v}^{\rho m} \cdot {}^{\text{t}}\mathbf{H}_{\rho\zeta}^{\rho m} + \mathbf{v}^{\rho m} \cdot \tilde{\mathbf{H}}_{\rho\zeta}^{\rho m} \quad (\text{D30})$$

$$\mathbf{v}^{\rho m} \cdot \tilde{\mathbf{H}}_{\rho\zeta}^{\rho m} = \begin{bmatrix} 2\epsilon_{\sigma_{mm}}^{\text{ot}} \sigma_{\zeta\zeta} & & & & \\ 2\epsilon_{\sigma_{mm}}^{\text{ot}} \sigma_{\rho\zeta} & 0 & & & \\ 0 & 0 & 0 & & \\ \epsilon_{\sigma_{\rho m}}^{\text{ot}} + 2\epsilon_{\sigma_{mm}}^{\text{ot}} \zeta & 2\epsilon_{\sigma_{mm}}^{\text{ot}} \rho & 0 & 0 & \\ 2\epsilon_{\sigma_{mm}}^{\text{ot}} \rho & 0 & 0 & 0 & 0 \end{bmatrix} \quad (\text{D31})$$

For the next transformation step to (ρ, R) , we must include the transformations for $\sigma_{\rho\zeta}$ and $\sigma_{\zeta\zeta}$ so that Eq. D21 is modified to be

$$\begin{bmatrix} \rho \\ \zeta \\ \sigma_{\rho\rho} \\ \sigma_{\rho\zeta} \\ \sigma_{\zeta\zeta} \end{bmatrix} = \begin{bmatrix} \rho \\ f(R) \\ \sigma_{\rho\rho} \\ f' \sigma_{\rho R} \\ (f')^2 \sigma_{RR} \end{bmatrix} \quad (\text{D32})$$

This leads to the modified Jacobian and Hessian as

$${}^{\text{ft}}\mathbf{J}_{\rho R}^{\rho\zeta} = {}^{\text{t}}\mathbf{J}_{\rho R}^{\rho\zeta} + \tilde{\mathbf{J}}_{\rho R}^{\rho\zeta} \quad (\text{D33})$$

$$\tilde{\mathbf{J}}_{\rho R}^{\rho\zeta} = \begin{bmatrix} 0 & 0 & 0 & 0 & 0 \\ 0 & 0 & 0 & 0 & 0 \\ 0 & 0 & 0 & 0 & 0 \\ 0 & \sigma_{\rho R} f'' & 0 & f' & 0 \\ 0 & 2\sigma_{RR} f'' f' & 0 & 0 & (f')^2 \end{bmatrix} \quad (\text{D34})$$

$$\mathbf{v}^{\rho\zeta} \cdot {}^{\text{ft}}\mathbf{H}_{\rho R}^{\rho\zeta} = \mathbf{v}^{\rho\zeta} \cdot {}^{\text{t}}\mathbf{H}_{\rho R}^{\rho\zeta} + \mathbf{v}^{\rho\zeta} \cdot \tilde{\mathbf{H}}_{\rho R}^{\rho\zeta} \quad (\text{D35})$$

$$\mathbf{v}^{\rho\zeta} \cdot \tilde{\mathbf{H}}_{\rho R}^{\rho\zeta} = \epsilon_{\sigma_{\rho\zeta}}^{\text{ot}} \mathbf{H}_{\rho R}^{\sigma_{\rho\zeta}} + \epsilon_{\sigma_{\zeta\zeta}}^{\text{ot}} \mathbf{H}_{\rho R}^{\sigma_{\zeta\zeta}} \quad (\text{D36})$$

where $\mathbf{H}_{\rho R}^{\sigma_{\rho\zeta}}$ and $\mathbf{H}_{\rho R}^{\sigma_{\zeta\zeta}}$ are the Hessians of $\sigma_{\rho\zeta}$ and $\sigma_{\zeta\zeta}$ with respect to the (ρ, R) variables.

$$\mathbf{H}_{\rho R}^{\sigma_{\rho\zeta}} = \begin{bmatrix} 0 & & & & \\ 0 & \sigma_{\rho R} f''' & & & \\ 0 & 0 & 0 & & \\ 0 & f'' & 0 & 0 & \\ 0 & 0 & 0 & 0 & 0 \end{bmatrix} \quad (\text{D37})$$

$$\mathbf{H}_{\rho R}^{\sigma_{\zeta\zeta}} = \begin{bmatrix} 0 & & & & \\ 0 & 2\sigma_{RR} (f''' f' + (f'')^2) & & & \\ 0 & 0 & 0 & & \\ 0 & 0 & 0 & 0 & 0 \\ 0 & 2f'' f' & & 0 & 0 & 0 \end{bmatrix} \quad (\text{D38})$$

The final transformation we must consider separately for the fully-translated functionals is to the (ρ, Π) coordinate. Here, we must include the transformation of the $\sigma_{\rho R}$ and σ_{RR} , which are not included in the translated case. The modified form of Eq. D24 for the fully-translated case is thus

$$\begin{bmatrix} \rho \\ R \\ \sigma_{\rho\rho} \\ \sigma_{\rho R} \\ \sigma_{RR} \end{bmatrix} = \begin{bmatrix} \rho \\ \frac{4\Pi}{\rho^2} \\ \sigma_{\rho\rho} \\ \frac{4}{\rho^2} (\sigma_{\rho\Pi} - \frac{2\Pi}{\rho} \sigma_{\rho\rho}) \\ \frac{16}{\rho^4} (\frac{4\Pi^2}{\rho^2} \sigma_{\rho\rho} - \frac{4\Pi}{\rho} \sigma_{\rho\Pi} + \sigma_{\Pi\Pi}) \end{bmatrix} \quad (\text{D39})$$

The fully-translated Jacobian is given by

$${}^{\text{ft}}\mathbf{J}_{\rho\Pi}^{\rho R} = {}^{\text{t}}\mathbf{J}_{\rho\Pi}^{\rho R} + \tilde{\mathbf{J}}_{\rho\Pi}^{\rho R} \quad (\text{D40})$$

$$\tilde{\mathbf{J}}_{\rho\Pi}^{\rho R} = \frac{4}{\rho^2} \begin{bmatrix} 0 & 0 & 0 & 0 & 0 \\ 0 & 0 & 0 & 0 & 0 \\ 0 & 0 & 0 & 0 & 0 \\ \frac{2}{\rho} \left(\frac{3\Pi\sigma_{\rho\rho}}{\rho} - \sigma_{\rho\Pi} \right) & -\frac{2\sigma_{\rho\rho}}{\rho} & -\frac{2\Pi}{\rho} & 1 & 0 \\ \frac{16}{\rho^3} \left(\frac{5\Pi\sigma_{\rho\Pi}}{\rho} - \frac{6\Pi^2\sigma_{\rho\rho}}{\rho^2} - \sigma_{\Pi\Pi} \right) & \frac{16}{\rho^3} \left(\frac{2\Pi\sigma_{\rho\rho}}{\rho} - \sigma_{\rho\Pi} \right) & \frac{16\Pi^2}{\rho^4} & -\frac{16\Pi}{\rho^3} & \frac{4}{\rho^2} \end{bmatrix} \quad (\text{D41})$$

And the fully-translated Hessian term is given by

$$\mathbf{v}^{\rho R} \cdot {}^{\text{ft}}\mathbf{H}_{\rho\Pi}^{\rho R} = \mathbf{v}^{\rho R} \cdot {}^{\text{t}}\mathbf{H}_{\rho\Pi}^{\rho R} + \mathbf{v}^{\rho R} \cdot \tilde{\mathbf{H}}_{\rho\Pi}^{\rho R} \quad (\text{D42})$$

$$\mathbf{v}^{\rho R} \cdot \tilde{\mathbf{H}}_{\rho\Pi}^{\rho R} = \epsilon_{\sigma_{\rho R}}^{\text{ot}} \mathbf{H}_{\rho\Pi}^{\sigma_{\rho R}} + \epsilon_{\sigma_{RR}}^{\text{ot}} \mathbf{H}_{\rho\Pi}^{\sigma_{RR}} \quad (\text{D43})$$

with $\mathbf{H}_{\rho\Pi}^{\sigma_{\rho R}}$ and $\mathbf{H}_{\rho\Pi}^{\sigma_{RR}}$ the Hessian of $\sigma_{\rho R}$ and σ_{RR} with

respect to the (ρ, Π) variables given by

$$\mathbf{H}_{\rho\Pi}^{\sigma_{\rho R}} = \begin{bmatrix} \frac{24}{\rho^3} (\sigma_{\rho\Pi} - R\sigma_{\rho\rho}) & & & & \\ \frac{24\sigma_{\rho\rho}}{\rho^4} & 0 & & & \\ \frac{6R}{\rho^2} & -\frac{8}{\rho^3} & 0 & & \\ -\frac{8}{\rho^3} & 0 & 0 & 0 & \\ 0 & 0 & 0 & 0 & 0 \end{bmatrix} \quad (\text{D44})$$

- put. **10**, 3669 (2014).
- [20] S. Ghosh, P. Verma, C. J. Cramer, L. Gagliardi, and D. G. Truhlar, Combining wave function methods with density functional theory for excited states, *Chem. Rev.* **118**, 7249 (2018).
- [21] C. Zhou, M. R. Hermes, D. Wu, J. J. Bao, R. Pandharkar, D. S. King, D. Zhang, T. R. Scott, A. O. Lykhin, L. Gagliardi, and D. G. Truhlar, Electronic structure of strongly correlated systems: recent developments in multiconfiguration pair-density functional theory and multiconfiguration nonclassical-energy functional theory, *Chem. Sci.* **13**, 7685 (2022).
- [22] C. E. Hoyer, S. Ghosh, D. G. Truhlar, and L. Gagliardi, Multiconfiguration pair-density functional theory is as accurate as CASPT2 for electronic excitation, *J. Phys. Chem. Lett.* **7**, 586 (2016).
- [23] D. S. King, M. R. Hermes, D. G. Truhlar, and L. Gagliardi, Large-scale benchmarking of multireference vertical-excitation calculations via automated active-space selection, *J. Chem. Theory Comput.* **18**, 6065 (2022).
- [24] A. M. Sand, C. E. Hoyer, D. G. Truhlar, and L. Gagliardi, State-interaction pair-density functional theory, *J. Chem. Phys.* **149**, 024106 (2018).
- [25] J. J. Bao, C. Zhou, Z. Varga, S. Kanchanakungwankul, L. Gagliardi, and D. G. Truhlar, Multi-state pair-density functional theory, *Faraday Discuss.* **224**, 348 (2020), 2003.06744v2.
- [26] J. J. Bao, C. Zhou, and D. G. Truhlar, Compressed-state multistate pair-density functional theory, *J. Chem. Theory Comput.* **16**, 7444 (2020).
- [27] M. R. Hennefarth, M. R. Hermes, D. G. Truhlar, and L. Gagliardi, Linearized pair-density functional theory, *J. Chem. Theory Comput.* **19**, 3172 (2023).
- [28] A. A. Granovsky, Extended multi-configuration quasi-degenerate perturbation theory: The new approach to multi-state multi-reference perturbation theory, *J. Chem. Phys.* **134**, 214113 (2011).
- [29] M. R. Hennefarth, D. S. King, and L. Gagliardi, Linearized pair-density functional theory for vertical excitation energies, *J. Chem. Theory Comput.* **19**, 7983 (2023).
- [30] J. Stålring, A. Bernhardsson, and R. Lindh, Analytical gradients of a state average MCSCF state and a state average diagnostic, *Mol. Phys.* **99**, 103 (2001).
- [31] A. M. Sand, C. E. Hoyer, K. Sharkas, K. M. Kidder, R. Lindh, D. G. Truhlar, and L. Gagliardi, Analytic gradients for complete active space pair-density functional theory, *J. Chem. Theory Comput.* **14**, 126 (2018), 1709.04985.
- [32] T. R. Scott, M. R. Hermes, A. M. Sand, M. S. Oakley, D. G. Truhlar, and L. Gagliardi, Analytic gradients for state-averaged multiconfiguration pair-density functional theory, *J. Chem. Phys.* **153**, 1 (2020).
- [33] T. R. Scott, M. S. Oakley, M. R. Hermes, A. M. Sand, R. Lindh, D. G. Truhlar, and L. Gagliardi, Analytic gradients for multiconfiguration pair-density functional theory with density fitting: Development and application to geometry optimization in the ground and excited states, *J. Chem. Phys.* **154**, 074108 (2021).
- [34] H. Hellmann, Zur rolle der kinetischen elektronenenergie für die zwischenatomaren kräfte, *Z. Phys* **85**, 180 (1933).
- [35] H. Hellmann, *Einführung in die quantenchemie* (Franz Deuticke, Leipzig und Wien, 1937).
- [36] R. P. Feynman, Forces in molecules, *Phys. Rev.* **56**, 340 (1939).
- [37] W. H. Press, S. A. Teukolsky, W. T. Vetterling, and B. P. Flannery, *Numerical recipes in Fortran 77: the art of scientific computing*, 2nd ed., Vol. 2 (Cambridge: Cambridge University Press, Cambridge, 1992).
- [38] A. Bernhardsson, R. Lindh, J. Olsen, and M. Fulscher, A direct implementation of the second-order derivatives of multiconfigurational SCF energies and an analysis of the preconditioning in the associated response equation, *Mol. Phys.* **96**, 617 (1999).
- [39] T. Helgaker, P. Jørgensen, and J. Olsen, *Molecular electronic-structure theory* (Wiley, Hoboken, 2014).
- [40] T. U. Helgaker and J. Almlöf, A second-quantization approach to the analytical evaluation of response properties for perturbation-dependent basis sets, *Int. J. Quantum Chem.* **26**, 275 (1984).
- [41] P.-O. Löwdin, On the non-orthogonality problem connected with the use of atomic wave functions in the theory of molecules and crystals, *J. Chem. Phys.* **18**, 365 (1950).
- [42] T. H. Dunning, Gaussian basis sets for use in correlated molecular calculations. I. the atoms boron through neon and hydrogen, *J. Chem. Phys.* **90**, 1007 (1989).
- [43] J. P. Perdew, K. Burke, and M. Ernzerhof, Generalized gradient approximation made simple, *Phys. Rev. Lett.* **77**, 3865 (1996).
- [44] R. K. Carlson, D. G. Truhlar, and L. Gagliardi, Multiconfiguration pair-density functional theory: A fully translated gradient approximation and its performance for transition metal dimers and the spectroscopy of $\text{Re}_2\text{Cl}_8^{2-}$, *J. Chem. Theory Comput.* **11**, 4077 (2015).
- [45] F. Bloch, Bemerkung zur elektronentheorie des ferromagnetismus und der elektrischen leitfähigkeit, *Z. Phys.* **57**, 545 (1929).
- [46] P. A. M. Dirac, Note on exchange phenomena in the Thomas atom, *Math. Proc. Cambridge Philos. Soc.* **26**, 376 (1930).
- [47] S. H. Vosko, L. Wilk, and M. Nusair, Accurate spin-dependent electron liquid correlation energies for local spin density calculations: a critical analysis, *Can. J. Phys.* **58**, 1200 (1980).
- [48] R. A. Kendall, T. H. Dunning, and R. J. Harrison, Electron affinities of the first-row atoms revisited. systematic basis sets and wave functions, *J. Chem. Phys.* **96**, 6796 (1992).
- [49] D. Feller, The role of databases in support of computational chemistry calculations, *J. Comput. Chem.* **17**, 1571 (1996).
- [50] K. L. Schuchardt, B. T. Didier, T. Elsethagen, L. Sun, V. Gurumoorthi, J. Chase, J. Li, and T. L. Windus, Basis set exchange: A community database for computational sciences, *J. Chem. Inf. Model.* **47**, 1045 (2007).
- [51] E. Papajak and D. G. Truhlar, Convergent partially augmented basis sets for post-Hartree-Fock calculations of molecular properties and reaction barrier heights, *J. Chem. Theory Comput.* **7**, 10 (2010).
- [52] P. Celani and H.-J. Werner, Analytical energy gradients for internally contracted second-order multireference perturbation theory, *J. Chem. Phys.* **119**, 5044 (2003).
- [53] Q. Sun, T. C. Berkelbach, N. S. Blunt, G. H. Booth, S. Guo, Z. Li, J. Liu, J. D. McClain, E. R. Sayfutyarova, S. Sharma, S. Wouters, and G. K. Chan, PySCF:

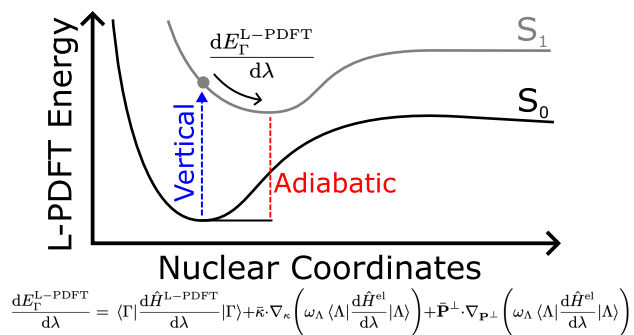
- The Python-based simulations of chemistry framework, *WIREs Comput. Mol. Sci.* **8**, e1340 (2017), 1701.08223.
- [54] Q. Sun, X. Zhang, S. Banerjee, P. Bao, M. Barbry, N. S. Blunt, N. A. Bogdanov, G. H. Booth, J. Chen, Z.-H. Cui, J. J. Eriksen, Y. Gao, S. Guo, J. Hermann, M. R. Hermes, K. Koh, P. Koval, S. Lehtola, Z. Li, J. Liu, N. Mardirossian, J. D. McClain, M. Motta, B. Mussard, H. Q. Pham, A. Pulkin, W. Purwanto, P. J. Robinson, E. Ronca, E. R. Sayfutyarova, M. Scheurer, H. F. Schurkus, J. E. T. Smith, C. Sun, S.-N. Sun, S. Upadhyay, L. K. Wagner, X. Wang, A. White, J. D. Whitfield, M. J. Williamson, S. Wouters, J. Yang, J. M. Yu, T. Zhu, T. C. Berkelbach, S. Sharma, A. Y. Sokolov, and G. K.-L. Chan, Recent developments in the PySCF program package, *J. Chem. Phys.* **153**, 024109 (2020), 2002.12531.
- [55] M. A. L. Marques, M. J. T. Oliveira, and T. Burnus, LIBXC: A library of exchange and correlation functionals for density functional theory, *Comput. Phys. Commun.* **183**, 2272 (2012), 1203.1739.
- [56] S. Lehtola, C. Steigemann, M. J. Oliveira, and M. A. Marques, Recent developments in LIBXC — a comprehensive library of functionals for density functional theory, *SoftwareX* **7**, 1 (2018).
- [57] Q. Sun, Libcint: An efficient general integral library for gaussian basis functions, *J. Comput. Chem.* **36**, 1664 (2015), 1412.0649.
- [58] M. R. Hermes, *MRH*, GitHub (2024).
- [59] *PySCF-FORGE*, GitHub (2024).
- [60] L.-P. Wang and C. Song, Geometry optimization made simple with translation and rotation coordinates, *J. Chem. Phys.* **144**, 214108 (2016).
- [61] J. J. Bao, M. R. Hermes, T. R. Scott, A. M. Sand, R. Lindh, L. Gagliardi, and D. G. Truhlar, Analytic gradients for compressed multistate pair-density functional theory, *Mol. Phys.* **120**, e2110534 (2022).
- [62] G. Glockler and D. L. Fuller, Helium hydride ion, *J. Chem. Phys.* **1**, 886 (1933).
- [63] D. M. Bishop and L. M. Cheung, A theoretical investigation of HeH^+ , *J. Mol. Spectrosc.* **75**, 462 (1979).
- [64] S. Peyerimhoff, Hartree–Fock–Roothaan wavefunctions, potential curves, and charge-density contours for the $\text{HeH}^+ (X^1\Sigma^+)$ and $\text{NeH}^+(X^1\Sigma^+)$ molecule ions, *J. Chem. Phys.* **43**, 998 (1965).
- [65] R. Güsten, H. Wiesemeyer, D. Neufeld, K. M. Menten, U. U. Graf, K. Jacobs, B. Klein, O. Ricken, C. Risacher, and J. Stutzki, Astrophysical detection of the helium hydride ion HeH^+ , *Nature* **568**, 357 (2019).
- [66] O. Novotný, P. Wilhelm, D. Paul, Á. Káloosi, S. Saurabh, A. Becker, K. Blaum, S. George, J. Göck, M. Grieser, F. Grussie, R. von Hahn, C. Krantz, H. Kreckel, C. Meyer, P. M. Mishra, D. Muell, F. Nuesslein, D. A. Orlov, M. Rimmler, V. C. Schmidt, A. Shornikov, A. S. Terekhov, S. Vogel, D. Zajfman, and A. Wolf, Quantum-state-selective electron recombination studies suggest enhanced abundance of primordial HeH^+ , *Science* **365**, 676 (2019).
- [67] R. J. Fallon, J. T. Vanderslice, and E. A. Mason, Potential energy curves for lithium hydride, *J. Chem. Phys.* **32**, 1453 (1960).
- [68] K. C. Li and W. C. Stwalley, The $A^1\Sigma^+ \rightarrow X^1\Sigma^+$ bands of the isotopic lithium hydrides, *J. Mol. Spectrosc.* **69**, 294 (1978).
- [69] A. Pardo, J. Camacho, and J. Poyato, The Padé-approximant method and its applications in the construction of potential-energy curves for the lithium hydride molecule, *Chem. Phys. Lett.* **131**, 490 (1986).
- [70] W. C. Stwalley and W. T. Zemke, Spectroscopy and structure of the lithium hydride diatomic molecules and ions, *J. Phys. Chem. Ref. Data* **22**, 87 (1993).
- [71] W.-C. Tung, M. Pavanello, and L. Adamowicz, Very accurate potential energy curve of the LiH molecule, *J. Chem. Phys.* **134**, 064117 (2011).
- [72] G. Li Manni, I. Fdez. Galván, A. Alavi, F. Aleotti, F. Aquilante, J. Autschbach, D. Avagliano, A. Baiardi, J. J. Bao, S. Battaglia, L. Birnoschi, A. Blanco-González, S. I. Bokarev, R. Broer, R. Cacciari, P. B. Calio, R. K. Carlson, R. Carvalho Couto, L. Cerdán, L. F. Chibotaru, N. F. Chilton, J. R. Church, I. Conti, S. Coriani, J. Cuéllar-Zuquin, R. E. Daoud, N. Dattani, P. Decleva, C. de Graaf, M. G. Delcey, L. De Vico, W. Dobrazt, S. S. Dong, R. Feng, N. Ferré, M. Filatov(Gulak), L. Gagliardi, M. Garavelli, L. González, Y. Guan, M. Guo, M. R. Hennefarth, M. R. Hermes, C. E. Hoyer, M. Huix-Rotllant, V. K. Jaiswal, A. Kaiser, D. S. Kaliakin, M. Khamesian, D. S. King, V. Kochetov, M. Krośnicki, A. A. Kumaar, E. D. Larsson, S. Lehtola, M.-B. Lepetit, H. Lischka, P. López Ríos, M. Lundberg, D. Ma, S. Mai, P. Marquetand, I. C. D. Merritt, F. Montorsi, M. Mörchen, A. Nenov, V. H. A. Nguyen, Y. Nishimoto, M. S. Oakley, M. Olivucci, M. Oppel, D. Padula, R. Pandharkar, Q. M. Phung, F. Plasser, G. Raggi, E. Rebolini, M. Reiher, I. Rivalta, D. Roca-Sanjuán, T. Romig, A. A. Safari, A. Sánchez-Mansilla, A. M. Sand, I. Schapiro, T. R. Scott, J. Segarra-Martí, F. Segatta, D.-C. Sergentu, P. Sharma, R. Shepard, Y. Shu, J. K. Staab, T. P. Straatsma, L. K. Sørensen, B. N. C. Tenorio, D. G. Truhlar, L. Ungur, M. Vacher, V. Veryazov, T. A. Voß, O. Weser, D. Wu, X. Yang, D. Yarkony, C. Zhou, J. P. Zobel, and R. Lindh, The OpenMolcas web: A community-driven approach to advancing computational chemistry, *J. Chem. Theory Comput.* **19**, 6933 (2023).
- [73] J. L. Duncan, The ground-state average and equilibrium structures of formaldehyde and ethylene, *Mol. Phys.* **28**, 1177 (1974).
- [74] P. Jensen and P. R. Bunker, The geometry and the inversion potential function of formaldehyde in the \tilde{A}^1A_2 and \tilde{a}^3A_2 electronic states, *J. Mol. Spectrosc.* **94**, 114 (1982).
- [75] Š. Budzák, G. Scalmani, and D. Jacquemin, Accurate excited-state geometries: a CASPT2 and coupled-cluster reference database for small molecules, *J. Chem. Theory Comput.* **13**, 6237 (2017).
- [76] J. J. Bao and D. G. Truhlar, Automatic active space selection for calculating electronic excitation energies based on high-spin unrestricted hartree–fock orbitals, *J. Chem. Theory Comput.* **15**, 5308 (2019).
- [77] A. Dreuw and M. Wormit, The algebraic diagrammatic construction scheme for the polarization propagator for the calculation of excited states, *WIREs Comput. Mol. Sci.* **5**, 82 (2014).
- [78] O. Christiansen, H. Koch, and P. Jørgensen, The second-order approximate coupled cluster singles and doubles model CC2, *Chem. Phys. Lett.* **243**, 409 (1995).

- [79] H. Koch, O. Christiansen, P. Jørgensen, A. M. Sanchez de Merás, and T. Helgaker, The CC3 model: An iterative coupled cluster approach including connected triples, *J. Chem. Phys.* **106**, 1808 (1997).
- [80] O. Christiansen, H. Koch, and P. Jørgensen, Perturbative triple excitation corrections to coupled cluster singles and doubles excitation energies, *J. Chem. Phys.* **105**, 1451 (1996).
- [81] P.-F. Loos, A. Scemama, A. Blondel, Y. Garniron, M. Caffarel, and D. Jacquemin, A mountaineering strategy to excited states: highly accurate reference energies and benchmarks, *J. Chem. Theory Comput.* **14**, 4360 (2018), 1807.02045.
- [82] K. N. Walzl, C. F. Koerting, and A. Kuppermann, Electron-impact spectroscopy of acetaldehyde, *J. Chem. Phys.* **87**, 3796 (1987).
- [83] P.-F. Loos, M. Boggio-Pasqua, A. Scemama, M. Caffarel, and D. Jacquemin, Reference Energies for Double Excitations, *J. Chem. Theory Comput.* **15**, 1939 (2019).
- [84] W. Haugen, M. Trættemberg, F. Kaufmann, K. Motzfeldt, D. H. Williams, E. Bunnenberg, C. Djerassi, and R. Records, The molecular structure of 1,3-butadiene and 1,3,5-trans-hexatriene., *Acta Chem. Scand.* **20**, 1726 (1966).
- [85] Y. Shu and D. G. Truhlar, Doubly excited character or static correlation of the reference state in the controversial 2^1A_g state of trans-butadiene?, *J. Am. Chem. Soc.* **139**, 13770 (2017).
- [86] M. A. Watson and G. K.-L. Chan, Excited states of butadiene to chemical accuracy: reconciling theory and experiment, *J. Chem. Theory Comput.* **8**, 4013 (2012).
- [87] J. Finley, P.-Å. Malmqvist, B. O. Roos, and L. Serrano-Andrés, The multi-state CASPT2 method, *Chem. Phys. Lett.* **288**, 299 (1998).
- [88] M. N. R. Ashfold, B. Cronin, A. L. Devine, R. N. Dixon, and M. G. D. Nix, The role of $\Pi\sigma^*$ excited states in the photodissociation of heteroaromatic molecules, *Science* **312**, 1637 (2006).
- [89] A. L. Devine, M. G. D. Nix, R. N. Dixon, and M. N. R. Ashfold, Near-ultraviolet photodissociation of thiophenol, *J. Phys. Chem. A* **112**, 9563 (2008).
- [90] M. N. R. Ashfold, A. L. Devine, R. N. Dixon, G. A. King, M. G. D. Nix, and T. A. A. Oliver, Exploring nuclear motion through conical intersections in the UV photodissociation of phenols and thiophenol, *Proc. Natl. Acad. Sci.* **105**, 12701 (2008).
- [91] J. S. Lim, H. Choi, I. S. Lim, S. B. Park, Y. S. Lee, and S. K. Kim, Photodissociation dynamics of thiophenol- d_1 : the nature of excited electronic states along the S-D bond dissociation coordinate, *J. Phys. Chem. A* **113**, 10410 (2009).
- [92] X. Xu, K. R. Yang, and D. G. Truhlar, Diabatic molecular orbitals, potential energies, and potential energy surface couplings by the 4-fold way for photodissociation of phenol, *J. Chem. Theory Comput.* **9**, 3612 (2013).
- [93] X. Zhu, C. L. Malbon, and D. R. Yarkony, An improved quasi-diabatic representation of the 1, 2, 3 1A coupled adiabatic potential energy surfaces of phenol in the full 33 internal coordinates, *J. Chem. Phys.* **144**, 124312 (2016).
- [94] L. Zhang, D. G. Truhlar, and S. Sun, Electronic spectrum and characterization of diabatic potential energy surfaces for thiophenol, *Phys. Chem. Chem. Phys.* **20**, 28144 (2018).
- [95] L. Zhang, D. G. Truhlar, and S. Sun, Full-dimensional three-state potential energy surfaces and state couplings for photodissociation of thiophenol, *J. Chem. Phys.* **151**, 154306 (2019).
- [96] N. W. Larsen, Microwave spectra of the six mono- ^{13}C -substituted phenols and of some monodeuterated species of phenol. Complete substitution structure and absolute dipole moment, *J. Mol. Struct.* **51**, 175 (1979).
- [97] D. Spangenberg, P. Imhof, and K. Kleinermanns, The S_1 state geometry of phenol determined by simultaneous Franck-Condon and rotational constants fits, *Phys. Chem. Chem. Phys.* **5**, 2505 (2003).
- [98] G. Granucci, J. T. Hynes, P. Millié, and T.-H. Tran-Thi, A theoretical investigation of excited-state acidity of phenol and cyanophenols, *J. Am. Chem. Soc.* **122**, 12243 (2000).
- [99] R. N. Dixon, T. A. A. Oliver, and M. N. R. Ashfold, Tunnelling under a conical intersection: Application to the product vibrational state distributions in the UV photodissociation of phenols, *J. Chem. Phys.* **134**, 194303 (2011).
- [100] G. A. Pino, A. N. Oldani, E. Marceca, M. Fujii, S.-I. Ishiuchi, M. Miyazaki, M. Broquier, C. Dedonder, and C. Jouvst, Excited state hydrogen transfer dynamics in substituted phenols and their complexes with ammonia: $\pi\pi^*$ - $\pi\sigma^*$ energy gap propensity and ortho-substitution effect, *J. Chem. Phys.* **133**, 124313 (2010).
- [101] O. P. J. Vieuxmaire, Z. Lan, A. L. Sobolewski, and W. Domcke, Ab initio characterization of the conical intersections involved in the photochemistry of phenol, *J. Chem. Phys.* **129**, 224307 (2008).
- [102] G. Fogarasi, Relative stabilities of three low-energy tautomers of cytosine: a coupled cluster correlation study, *J. Phys. Chem. A* **106**, 1381 (2002).
- [103] D. L. Barker and R. E. Marsh, The crystal structure of cytosine, *Acta Crystallogr.* **17**, 1581 (1964).
- [104] A. Nakayama, S. Yamazaki, and T. Taketsugu, Quantum chemical investigations on the nonradiative deactivation pathways of cytosine derivatives, *J. Phys. Chem. A* **118**, 9429 (2014).
- [105] Chr. Møller and M. S. Plesset, Note on an approximation treatment for many-electron systems, *Phys. Rev.* **46**, 618 (1934).
- [106] M. Head-Gordon, J. A. Pople, and M. J. Frisch, MP2 energy evaluation by direct methods, *Chem. Phys. Lett.* **153**, 503 (1988).
- [107] P. J. Knowles and H.-J. Werner, Internally contracted multiconfiguration-reference configuration interaction calculations for excited states, *Theoret. Chim. Acta* **84**, 95 (1992).
- [108] M. Merchán, R. González-Luque, T. Climent, L. Serrano-Andrés, E. Rodríguez, M. Reguero, and D. Peláez, Unified model for the ultrafast decay of pyrimidine nucleobases, *J. Phys. Chem. B* **110**, 26471 (2006).
- [109] J. González-Vázquez and L. González, A time-dependent picture of the ultrafast deactivation of keto-cytosine including three-state conical intersections, *ChemPhysChem* **11**, 3617 (2010).
- [110] A. Nakayama, Y. Harabuchi, S. Yamazaki, and T. Taketsugu, Photophysics of cytosine tautomers: new insights into the nonradiative decay mechanisms from MS-CASPT2 potential energy calculations and excited-state molecular dynamics simulations, *Phys. Chem.*

[Chem. Phys. 15, 12322 \(2013\)](#).

- [111] T. D. Cherneva, M. M. Todorova, R. I. Bakalska, I. G. Shterev, E. Horkel, and V. B. Delchev, Experimental and theoretical study of the cytosine tautomerism through excited states, [J. Mol. Model. 29, 303 \(2023\)](#).
- [112] R. Abouaf, J. Pommier, H. Dunet, P. Quan, P.-C. Nam, and M. T. Nguyen, The triplet state of cytosine and its derivatives: Electron impact and quantum chemical study, [J. Chem. Phys. 121, 11668 \(2004\)](#).

TOC GRAPHIC



Supplementary Material: Analytic Nuclear Gradients for Complete Active Space Linearized Pair-Density Functional Theory

Matthew R. Hennefarth,¹ Matthew R. Hermes,¹ Donald G. Truhlar,^{2,*} and Laura Gagliardi^{3,4,†}

¹Department of Chemistry and Chicago Center for Theoretical Chemistry, University of Chicago, Chicago, IL 60637, USA

²Department of Chemistry, Chemical Theory Center, and Minnesota Supercomputing Institute, University of Minnesota, Minneapolis, MN 55455-0431, USA

³Department of Chemistry, Pritzker School of Molecular Engineering, The James Franck Institute, and Chicago Center for Theoretical Chemistry, University of Chicago, Chicago, IL 60637, USA

⁴Argonne National Laboratory, 9700 S. Cass Avenue, Lemont, IL 60439, USA

(Dated: March 14, 2024)

CONTENTS

SI. Supplemental Figures	S1
SII. Optimized Geometries	S3
A. Formaldehyde	S3
B. Phenol	S4
C. <i>Trans</i> -butadiene	S4
D. Cytosine	S5
SIII. Absolute Gradients	S6

SI. SUPPLEMENTAL FIGURES

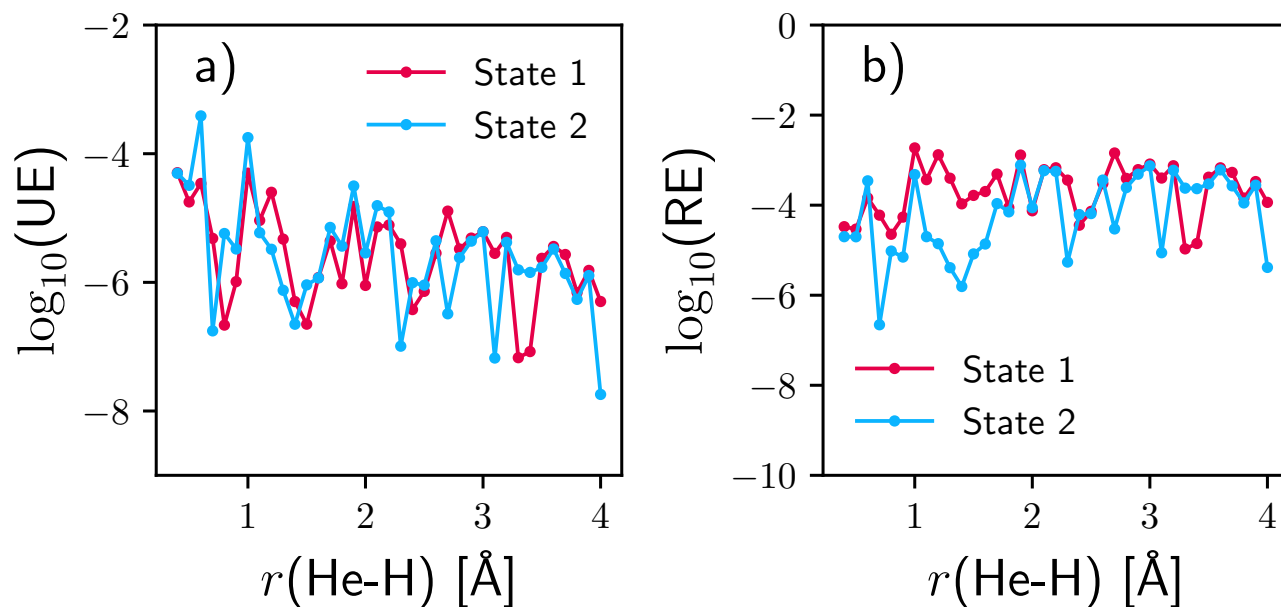


FIG. S1. Log unsigned (a) and relative (b) error for HeH⁺ computed with the tPBE functional at various He-H distances.

* corresponding author: truhlar@umn.edu

† corresponding author: lgagliardi@uchicago.edu

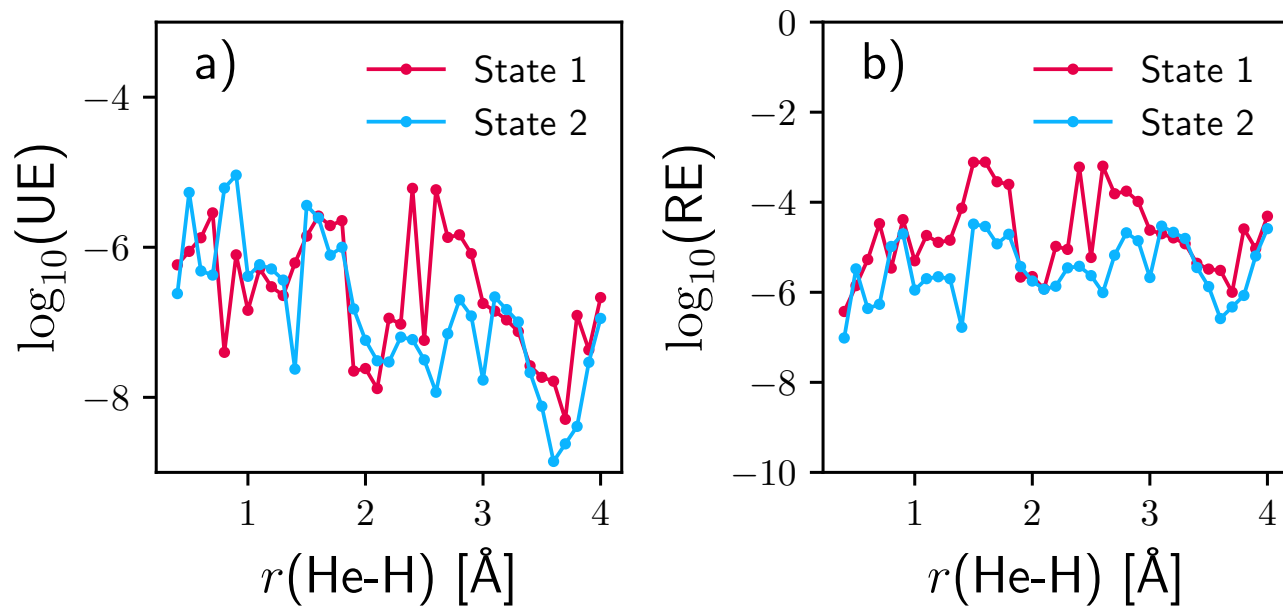


FIG. S2. Log unsigned (a) and relative (b) error for HeH⁺ computed with the ftSVWN3 functional at various He-H distances.

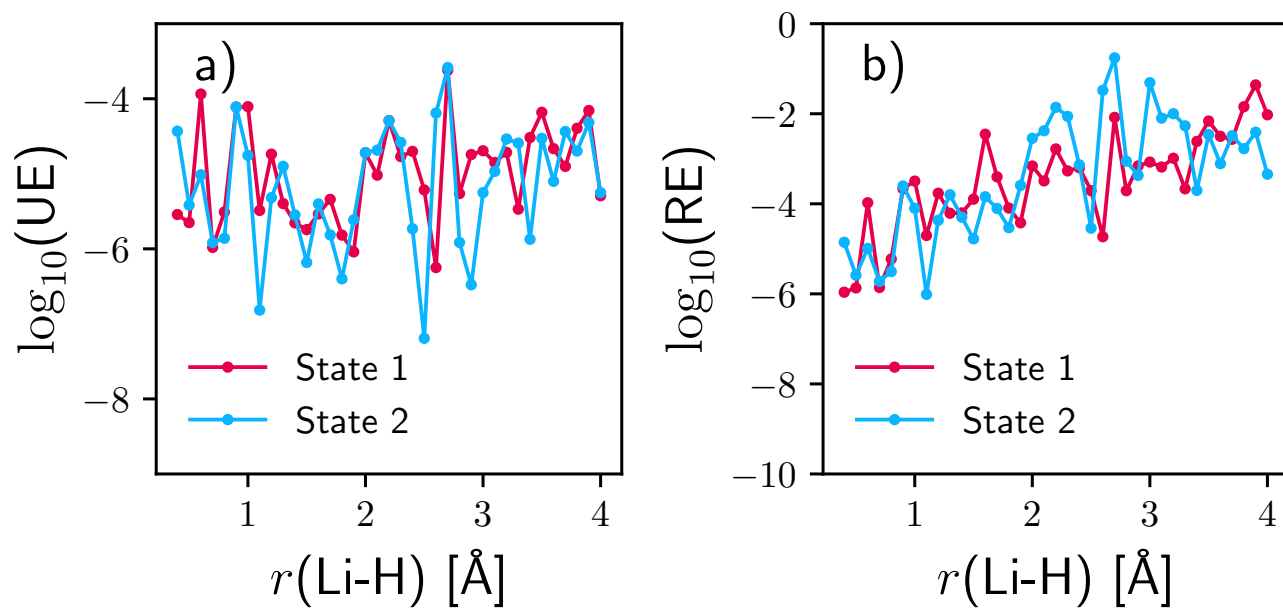


FIG. S3. Log unsigned (a) and relative (b) error for LiH computed with the tPBE functional at various Li-H distances.

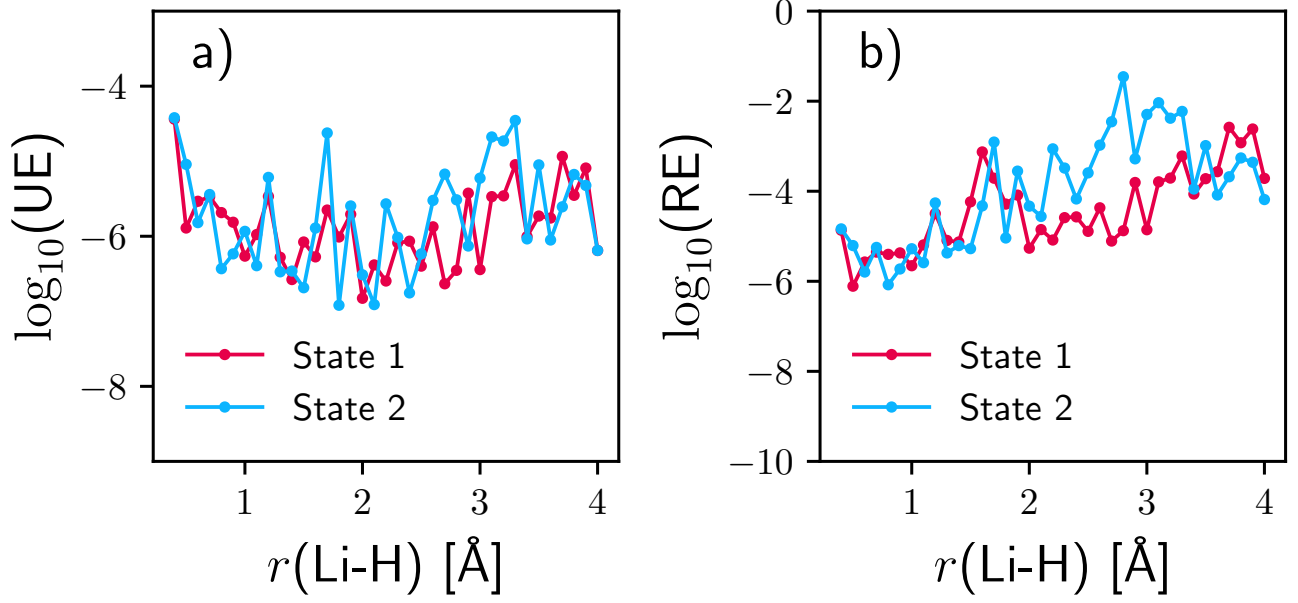


FIG. S4. Log unsigned (a) and relative (b) error for LiH computed with the ftPBE functional at various Li-H distances.

SII. OPTIMIZED GEOMETRIES

A. Formaldehyde

TABLE SI. L-PDFT formaldehyde equilibrium ground state geometry (in Å). State 0 energy: $-114.383\,708\,39$ hartree. State 1 energy: $-114.237\,395\,37$ hartree

C	0.49586	-0.00001	-0.00001
O	-0.71370	0.00001	-0.00004
H	1.08345	-0.00000	0.94756
H	1.08356	0.00000	-0.94751

TABLE SII. L-PDFT formaldehyde equilibrium excited state geometry (in Å). State 0 energy: $-114.355\,724\,79$ hartree. State 1 energy: $-114.250\,986\,75$ hartree

C	0.50356	-0.02576	-0.00008
O	-0.64094	0.64726	-0.00003
H	1.06843	0.01424	0.94321
H	1.06836	0.01426	-0.94341

B. Phenol

TABLE SIII. L-PDFT phenol equilibrium ground state geometry (in Å). State 0 energy: $-307.061\,573\,88$ hartree. State 1 energy: $-306.876\,565\,79$ hartree. State 2 energy: $-306.859\,271\,28$ hartree.

C	1.26641	0.00000	2.08922
C	2.48510	0.00000	1.39749
C	2.47503	-0.00000	-0.00203
C	1.26674	-0.00000	-0.70531
C	0.05247	-0.00000	-0.00139
C	0.05113	-0.00000	1.40115
O	-1.16160	-0.00000	-0.63308
H	3.42040	-0.00000	-0.55945
H	3.43496	0.00000	1.94523
H	1.25970	0.00000	3.18668
H	-0.90866	0.00000	1.93095
H	1.26439	-0.00000	-1.80482
H	-1.02640	0.00000	-1.58516

TABLE SIV. L-PDFT phenol equilibrium first excited state geometry (in Å). State 0 energy: $-307.054\,612\,58$ hartree. State 1 energy: $-306.883\,396\,67$ hartree. State 2 energy: $-306.858\,666\,71$ hartree.

C	1.25874	0.00000	2.13850
C	2.47518	0.00000	1.39403
C	2.50474	0.00000	-0.03457
C	1.26890	0.00000	-0.75821
C	0.05105	-0.00000	0.00454
C	0.00947	-0.00000	1.43296
O	-1.13755	-0.00000	-0.62615
H	3.46259	0.00000	-0.56442
H	3.42850	0.00000	1.93823
H	1.28146	0.00000	3.23263
H	-0.96178	-0.00000	1.93597
H	1.23317	0.00000	-1.85461
H	-0.99479	-0.00000	-1.57942

C. *Trans*-butadiene

TABLE SV. L-PDFT *trans*-butadiene equilibrium ground state (1^1A_g) geometry (in Å). 1^1A_g energy: $-155.787\,113\,61$ hartree. 2^1A_g energy: $-155.532\,936\,52$ hartree.

C	1.16325	0.00002	-1.43351
C	0.02896	-0.00001	-0.72932
C	-0.02896	0.00001	0.72932
C	-1.16325	-0.00002	1.43351
H	-0.93173	-0.00004	-1.25031
H	1.16211	0.00001	-2.52157
H	2.13664	0.00006	-0.94202
H	0.93173	0.00004	1.25031
H	-1.16211	-0.00001	2.52157
H	-2.13664	-0.00006	0.94202

TABLE SVI. L-PDFT *trans*-butadiene equilibrium 2^1A_g state geometry (in Å). 1^1A_g energy: -155.74867922 hartree. 2^1A_g energy: -155.57485703 hartree.

C	1.26795	0.00003	-1.51460
C	0.01332	-0.00001	-0.69913
C	-0.01332	0.00001	0.69913
C	-1.26795	-0.00003	1.51460
H	-0.93183	-0.00004	-1.24190
H	1.21814	0.00002	-2.59769
H	2.24001	0.00006	-1.03038
H	0.93183	0.00004	1.24190
H	-1.21814	-0.00002	2.59769
H	-2.24001	-0.00006	1.03038

D. Cytosine

TABLE SVII. L-PDFT cytosine equilibrium ground state ($1^1A'$) geometry (in Å). $1^1A'$ energy: -394.55508466 hartree. $2^1A'$ energy: -394.39281789 hartree. $3^1A'$ energy: -394.36098028 hartree.

C	1.04984	1.19134	-0.00416
C	1.13724	-0.23990	-0.00508
N	0.08654	-1.05068	-0.00078
C	-1.17747	-0.54080	0.00496
N	-1.27884	0.89327	0.00595
C	-0.20931	1.70775	0.00157
N	2.35051	-0.83542	-0.01063
O	-2.21720	-1.17514	0.00929
H	-2.22563	1.25388	0.01024
H	-0.40459	2.77816	0.00283
H	1.92547	1.83177	-0.00776
H	3.20773	-0.30568	-0.01419
H	2.38152	-1.84599	-0.01115

TABLE SVIII. L-PDFT cytosine equilibrium $2^1A'$ state geometry (in Å). $1^1A'$ energy: -394.53676415 hartree. $2^1A'$ energy: -394.4062025 hartree. $3^1A'$ energy: -394.36145003 hartree.

C	1.05299	1.18617	-0.00417
C	1.18415	-0.18352	-0.00527
N	0.07770	-1.05043	-0.00074
C	-1.11395	-0.49925	0.00470
N	-1.30540	0.88580	0.00606
C	-0.23454	1.77191	0.00170
N	2.36308	-0.86413	-0.01070
O	-2.19194	-1.17166	0.00918
H	-2.27061	1.19130	0.01042
H	-0.43974	2.83438	0.00300
H	1.92625	1.83475	-0.00776
H	3.25747	-0.39974	-0.01445
H	2.32035	-1.87302	-0.01089

SIII. ABSOLUTE GRADIENTS

TABLE SIX. Analytical and extrapolated numerical gradients (hartree/bohr) for HeH⁺ with the tPBE functional at various He-H distances (Å).

R	Analytic		Numeric (extrapolated)	
	State 1	State 2	State 1	State 2
0.4	-1.522 646 953 2	-2.486 423 975 4	-1.522 596 295 6	-2.486 473 568 7
0.5	-0.605 279 221 2	-1.623 800 260 8	-0.605 261 433 5	-1.623 832 496 6
0.6	-0.238 770 053 1	-1.114 897 756 4	-0.238 804 517 6	-1.115 284 612 5
0.7	-0.080 528 906 6	-0.797 818 359 7	-0.080 524 079 2	-0.797 818 535 8
0.8	-0.009 587 749 3	-0.601 328 641 1	-0.009 587 532 9	-0.601 322 896 5
0.9	0.018 892 226 5	-0.469 383 301 2	0.018 891 201 0	-0.469 379 998 1
1.0	0.026 611 957 6	-0.372 302 456 2	0.026 661 753 5	-0.372 124 575 1
1.1	0.024 903 999 2	-0.296 176 367 9	0.024 913 180 5	-0.296 182 277 7
1.2	0.019 056 394 9	-0.234 403 292 1	0.019 081 525 7	-0.234 406 560 0
1.3	0.011 841 179 5	-0.184 048 965 3	0.011 845 877 8	-0.184 049 717 4
1.4	0.004 695 761 3	-0.143 022 413 1	0.004 696 263 9	-0.143 022 636 4
1.5	-0.001 359 027 0	-0.110 519 255 6	-0.001 358 803 3	-0.110 520 168 7
1.6	-0.005 905 877 0	-0.085 261 328 2	-0.005 907 063 5	-0.085 260 159 3
1.7	-0.008 957 175 2	-0.065 962 168 8	-0.008 961 576 2	-0.065 955 025 7
1.8	-0.010 752 488 6	-0.051 549 748 6	-0.010 753 442 0	-0.051 546 090 0
1.9	-0.011 669 835 1	-0.040 649 970 9	-0.011 654 712 2	-0.040 681 429 4
2.0	-0.011 947 132 2	-0.032 629 640 9	-0.011 948 028 0	-0.032 626 770 0
2.1	-0.011 842 807 0	-0.026 624 851 9	-0.011 835 538 6	-0.026 640 423 0
2.2	-0.011 498 813 5	-0.022 105 389 5	-0.011 506 600 3	-0.022 092 961 7
2.3	-0.011 024 610 0	-0.018 684 546 4	-0.011 020 644 5	-0.018 684 444 6
2.4	-0.010 506 099 8	-0.015 998 139 5	-0.010 506 477 2	-0.015 997 151 8
2.5	-0.009 958 439 4	-0.013 926 051 2	-0.009 957 714 5	-0.013 926 956 6
2.6	-0.009 420 657 3	-0.012 273 843 1	-0.009 417 817 5	-0.012 278 273 7
2.7	-0.008 896 813 9	-0.010 944 107 3	-0.008 884 009 2	-0.010 943 782 7
2.8	-0.008 404 678 0	-0.009 857 455 3	-0.008 407 977 5	-0.009 859 875 5
2.9	-0.007 925 898 8	-0.008 965 480 7	-0.007 921 025 1	-0.008 969 851 7
3.0	-0.007 488 413 3	-0.008 210 202 2	-0.007 494 546 0	-0.008 204 077 1
3.1	-0.007 061 931 8	-0.007 582 267 7	-0.007 059 107 7	-0.007 582 201 1
3.2	-0.006 675 773 3	-0.007 027 773 3	-0.006 670 769 4	-0.007 031 959 4
3.3	-0.006 311 853 3	-0.006 552 288 6	-0.006 311 920 7	-0.006 553 852 8
3.4	-0.005 965 111 6	-0.006 136 730 4	-0.005 965 195 5	-0.006 138 158 1
3.5	-0.005 655 025 6	-0.005 757 088 9	-0.005 657 389 7	-0.005 755 382 0
3.6	-0.005 357 111 5	-0.005 426 174 7	-0.005 353 498 5	-0.005 429 476 0
3.7	-0.005 081 257 7	-0.005 124 264 2	-0.005 078 547 7	-0.005 125 638 3
3.8	-0.004 825 693 3	-0.004 849 442 8	-0.004 824 999 8	-0.004 849 986 6
3.9	-0.004 589 006 3	-0.004 596 985 7	-0.004 587 473 3	-0.004 598 261 4
4.0	-0.004 366 106 4	-0.004 367 380 5	-0.004 365 602 9	-0.004 367 398 6

TABLE SX. Analytical and extrapolated numerical gradients (hartree/bohr) for HeH⁺ with the ftSVWN3 functional at various He-H distances (Å).

R	Analytic		Numeric (extrapolated)	
	State 1	State 2	State 1	State 2
0.4	-1.557 501 131 8	-2.497 799 710 6	-1.557 501 714 7	-2.497 799 952 0
0.5	-0.627 890 396 8	-1.620 233 006 1	-0.627 891 278 7	-1.620 238 368 6
0.6	-0.251 008 731 0	-1.106 732 564 4	-0.251 010 068 9	-1.106 732 080 9
0.7	-0.085 997 745 6	-0.787 912 840 2	-0.085 994 875 5	-0.787 912 414 1
0.8	-0.011 541 008 3	-0.590 636 298 8	-0.011 540 968 5	-0.590 630 148 5
0.9	0.019 300 220 4	-0.460 293 855 3	0.019 301 012 3	-0.460 284 710 5
1.0	0.028 903 035 7	-0.365 943 110 3	0.028 902 891 1	-0.365 942 700 5
1.1	0.028 367 354 6	-0.292 093 626 2	0.028 366 836 9	-0.292 094 211 7
1.2	0.023 138 959 6	-0.232 098 214 1	0.023 138 662 0	-0.232 098 727 6
1.3	0.015 905 260 6	-0.182 741 758 9	0.015 905 488 4	-0.182 742 123 9
1.4	0.008 385 580 1	-0.142 470 337 6	0.008 384 961 6	-0.142 470 361 4
1.5	0.001 825 981 7	-0.110 361 700 9	0.001 824 575 0	-0.110 358 091 7
1.6	-0.003 344 678 0	-0.085 157 603 7	-0.003 347 280 5	-0.085 155 137 3
1.7	-0.006 835 200 7	-0.065 945 754 3	-0.006 837 147 9	-0.065 944 969 9
1.8	-0.009 063 157 1	-0.051 423 162 5	-0.009 065 417 9	-0.051 422 162 5
1.9	-0.010 305 516 2	-0.040 508 262 7	-0.010 305 493 8	-0.040 508 413 6
2.0	-0.010 845 460 1	-0.032 413 169 0	-0.010 845 484 3	-0.032 413 226 6
2.1	-0.011 004 155 8	-0.026 286 425 1	-0.011 004 168 9	-0.026 286 455 8
2.2	-0.010 827 210 5	-0.021 731 659 3	-0.010 827 097 3	-0.021 731 688 9
2.3	-0.010 544 143 5	-0.018 226 705 6	-0.010 544 238 1	-0.018 226 642 1
2.4	-0.010 125 121 1	-0.015 571 915 4	-0.010 119 028 0	-0.015 571 974 2
2.5	-0.009 690 538 7	-0.013 496 255 6	-0.009 690 596 2	-0.013 496 224 0
2.6	-0.009 224 673 1	-0.011 880 529 6	-0.009 230 503 2	-0.011 880 541 3
2.7	-0.008 773 165 5	-0.010 582 935 1	-0.008 774 520 1	-0.010 583 005 6
2.8	-0.008 322 253 6	-0.009 543 437 1	-0.008 320 788 4	-0.009 543 636 8
2.9	-0.007 883 532 7	-0.008 692 276 0	-0.007 882 712 1	-0.008 692 397 3
3.0	-0.007 457 997 3	-0.007 989 368 9	-0.007 457 819 0	-0.007 989 351 9
3.1	-0.007 053 659 5	-0.007 392 761 3	-0.007 053 518 4	-0.007 392 979 1
3.2	-0.006 672 050 0	-0.006 879 457 6	-0.006 671 942 3	-0.006 879 605 3
3.3	-0.006 309 709 6	-0.006 434 638 8	-0.006 309 634 2	-0.006 434 739 8
3.4	-0.005 971 705 9	-0.006 040 199 8	-0.005 971 732 2	-0.006 040 221 2
3.5	-0.005 655 862 5	-0.005 687 592 1	-0.005 655 881 0	-0.005 687 599 7
3.6	-0.005 360 007 5	-0.005 370 949 0	-0.005 360 023 9	-0.005 370 947 6
3.7	-0.005 085 148 8	-0.005 081 911 2	-0.005 085 143 7	-0.005 081 913 6
3.8	-0.004 829 026 6	-0.004 817 892 4	-0.004 828 903 3	-0.004 817 896 5
3.9	-0.004 590 120 9	-0.004 575 269 1	-0.004 590 163 8	-0.004 575 298 4
4.0	-0.004 367 752 1	-0.004 350 696 7	-0.004 367 965 6	-0.004 350 584 1

TABLE SXI. Analytical and extrapolated numerical gradients (hartree/bohr) for LiH with the tPBE functional at various Li-H distances (Å).

R	Analytic		Numeric (extrapolated)	
	State 1	State 2	State 1	State 2
0.4	-2.632 302 524 9	-2.640 660 292 4	-2.632 299 660 5	-2.640 623 318 8
0.5	-1.650 210 726 1	-1.471 546 843 0	-1.650 208 493 3	-1.471 550 663 9
0.6	-1.095 749 768 0	-0.944 700 369 2	-1.095 634 060 1	-0.944 710 066 2
0.7	-0.753 584 800 1	-0.639 256 904 0	-0.753 585 844 2	-0.639 255 690 6
0.8	-0.521 309 649 3	-0.443 153 776 6	-0.521 312 749 0	-0.443 152 394 2
0.9	-0.359 902 821 7	-0.311 719 010 5	-0.359 825 229 2	-0.311 796 526 6
1.0	-0.245 596 399 1	-0.220 797 368 7	-0.245 517 960 8	-0.220 814 958 2
1.1	-0.164 234 639 5	-0.156 832 041 2	-0.164 231 392 4	-0.156 832 193 7
1.2	-0.106 307 136 8	-0.111 458 526 9	-0.106 288 873 3	-0.111 463 336 2
1.3	-0.064 942 606 3	-0.079 076 999 6	-0.064 946 614 6	-0.079 089 567 1
1.4	-0.035 359 641 0	-0.055 940 462 4	-0.035 357 421 7	-0.055 943 285 7
1.5	-0.014 222 716 1	-0.039 413 107 8	-0.014 220 913 0	-0.039 413 765 5
1.6	0.000 835 263 4	-0.027 664 730 6	0.000 832 342 4	-0.027 668 699 6
1.7	0.011 487 043 1	-0.019 344 057 0	0.011 491 609 6	-0.019 342 525 9
1.8	0.018 943 166 9	-0.013 504 237 3	0.018 941 643 2	-0.013 504 635 6
1.9	0.024 074 653 7	-0.009 463 293 6	0.024 075 564 3	-0.009 460 863 8
2.0	0.027 518 764 0	-0.006 747 563 7	0.027 499 739 3	-0.006 728 370 4
2.1	0.029 692 613 0	-0.004 897 191 0	0.029 702 197 8	-0.004 917 815 0
2.2	0.030 944 224 1	-0.003 718 621 4	0.030 893 118 4	-0.003 667 615 7
2.3	0.031 489 696 4	-0.002 965 468 4	0.031 506 651 5	-0.002 991 658 4
2.4	0.031 500 121 6	-0.002 531 567 6	0.031 520 012 4	-0.002 529 716 9
2.5	0.031 076 053 4	-0.002 231 561 6	0.031 069 960 6	-0.002 231 625 8
2.6	0.030 297 713 7	-0.002 010 439 7	0.030 298 276 4	-0.001 945 971 6
2.7	0.029 201 288 5	-0.001 753 156 9	0.028 960 792 0	-0.001 492 559 9
2.8	0.027 802 317 9	-0.001 377 203 3	0.027 807 762 2	-0.001 375 987 7
2.9	0.026 068 986 3	-0.000 777 542 8	0.026 050 940 7	-0.000 777 875 2
3.0	0.023 995 167 4	0.000 119 880 6	0.023 974 897 0	0.000 114 274 2
3.1	0.021 555 677 7	0.001 357 748 9	0.021 569 825 3	0.001 346 985 2
3.2	0.018 764 719 5	0.002 934 300 5	0.018 745 447 6	0.002 905 219 7
3.3	0.015 706 246 6	0.004 791 510 4	0.015 702 868 9	0.004 765 852 6
3.4	0.012 549 071 9	0.006 764 481 9	0.012 518 659 1	0.006 765 821 9
3.5	0.009 521 593 9	0.008 625 268 5	0.009 587 561 3	0.008 595 565 9
3.6	0.006 841 696 2	0.010 161 995 7	0.006 863 310 3	0.010 169 925 3
3.7	0.004 618 247 8	0.011 271 297 5	0.004 630 799 6	0.011 234 740 6
3.8	0.002 862 935 7	0.011 952 761 5	0.002 822 516 3	0.011 972 861 0
3.9	0.001 528 523 5	0.012 276 839 7	0.001 598 261 2	0.012 324 841 3
4.0	0.000 532 973 2	0.012 328 572 6	0.000 538 074 0	0.012 322 970 0

TABLE SXII. Analytical and extrapolated numerical gradients (hartree/bohr) for LiH with the ftPBE functional at various Li-H distances (Å).

R	Analytic		Numeric (extrapolated)	
	State 1	State 2	State 1	State 2
0.4	-2.666 609 778 0	-2.604 440 722 4	-2.666 646 120 5	-2.604 402 772 9
0.5	-1.655 789 280 5	-1.461 090 276 5	-1.655 787 992 4	-1.461 081 203 1
0.6	-1.092 133 086 7	-0.946 460 476 7	-1.092 130 161 5	-0.946 461 996 8
0.7	-0.754 310 517 4	-0.636 796 492 1	-0.754 313 870 8	-0.636 792 894 5
0.8	-0.521 212 050 1	-0.441 707 445 5	-0.521 209 984 2	-0.441 707 075 9
0.9	-0.359 816 809 4	-0.310 668 512 5	-0.359 815 272 5	-0.310 669 095 0
1.0	-0.245 489 742 8	-0.220 106 172 3	-0.245 489 199 3	-0.220 107 334 8
1.1	-0.163 998 080 1	-0.156 529 459 3	-0.163 997 026 7	-0.156 529 054 0
1.2	-0.106 493 906 9	-0.110 928 046 9	-0.106 490 507 9	-0.110 921 960 0
1.3	-0.064 972 306 1	-0.078 857 221 2	-0.064 971 781 4	-0.078 857 557 0
1.4	-0.035 554 362 8	-0.055 496 473 8	-0.035 554 627 8	-0.055 496 129 9
1.5	-0.014 412 052 7	-0.038 865 367 7	-0.014 411 214 3	-0.038 865 161 6
1.6	0.000 712 345 1	-0.027 201 225 1	0.000 711 814 2	-0.027 199 938 2
1.7	0.011 481 482 4	-0.019 284 670 3	0.011 483 716 8	-0.019 260 884 1
1.8	0.018 846 130 9	-0.013 152 887 8	0.018 845 153 5	-0.013 153 008 2
1.9	0.023 948 745 6	-0.009 063 535 4	0.023 950 708 7	-0.009 066 069 6
2.0	0.027 433 565 6	-0.006 570 579 0	0.027 433 714 7	-0.006 570 885 2
2.1	0.029 515 482 6	-0.004 457 860 6	0.029 515 897 5	-0.004 457 983 4
2.2	0.030 689 411 6	-0.003 091 763 4	0.030 689 158 3	-0.003 094 465 9
2.3	0.031 560 811 1	-0.002 955 148 3	0.031 561 628 6	-0.002 956 115 0
2.4	0.031 913 878 9	-0.002 609 623 6	0.031 913 019 5	-0.002 609 799 4
2.5	0.031 109 745 7	-0.002 275 173 8	0.031 109 345 8	-0.002 274 592 4
2.6	0.031 178 166 2	-0.002 844 308 2	0.031 179 501 7	-0.002 847 312 3
2.7	0.029 716 258 7	-0.001 920 663 6	0.029 716 491 2	-0.001 927 390 2
2.8	0.026 413 799 0	0.000 090 825 3	0.026 413 447 7	0.000 087 764 6
2.9	0.024 012 596 7	0.001 414 572 6	0.024 008 844 8	0.001 415 314 0
3.0	0.025 751 901 5	-0.001 165 358 5	0.025 751 541 9	-0.001 171 304 0
3.1	0.020 883 199 1	0.002 298 971 5	0.020 879 827 0	0.002 277 925 7
3.2	0.017 614 533 0	0.004 467 897 3	0.017 617 984 9	0.004 449 284 0
3.3	0.014 833 667 4	0.005 930 455 0	0.014 842 651 8	0.005 895 537 7
3.4	0.011 435 180 2	0.008 223 996 8	0.011 436 170 8	0.008 224 919 3
3.5	0.009 788 017 3	0.008 677 567 6	0.009 789 876 1	0.008 668 636 8
3.6	0.006 440 920 8	0.010 804 771 0	0.006 439 171 9	0.010 805 662 5
3.7	0.004 393 403 3	0.011 788 470 0	0.004 404 985 1	0.011 786 000 7
3.8	0.002 941 335 9	0.012 152 223 7	0.002 944 848 2	0.012 145 565 7
3.9	0.003 372 609 2	0.010 816 123 2	0.003 364 498 8	0.010 820 881 1
4.0	0.003 350 342 7	0.009 904 076 9	0.003 349 696 7	0.009 904 723 8